A Performance Analysis of a Direct-Conversion Digital X-ray Imager

by

Amith Kumar Salhotra

A THESIS SUBMITTED IN PARTIAL FULFILLMENT OF
THE REQUIREMENTS FOR THE DEGREE OF

MASTER OF APPLIED SCIENCE

in

THE COLLEGE OF GRADUATE STUDIES

(Electrical Engineering)

THE UNIVERSITY OF BRITISH COLUMBIA

(Okanagan)

September 2014

Abstract

In this thesis, the performance of direct-conversion digital X-ray imagers is evaluated using an elementary model that draws upon the material properties and the dimensions of the X-ray photoconductor employed within such imagers. Five possible X-ray photoconductors are considered in this analysis, namely amorphous selenium, cadmium zinc telluride, mercury iodide, lead iodide, and thallium bromide. The collected charge per unit area is the performance metric considered in this analysis. The collected charge per unit area related to the motion of the electrons and holes individually, and due the motion of both types of charge carriers, is evaluated. The fractional contributions to the collected charge per unit area is also evaluated. The application of both positive and negative biases to the radiation receiving terminals is considered. It is found that the collected charge per unit area, for the case of both positive and negative biases, is higher for the case of cadmium zinc telluride when compared with the other X-ray photoconductors considered in this analysis. This suggests that cadmium zinc telluride may be a better material to employ as the X-ray photoconductor within direct-conversion digital X-ray imagers.

Table of Contents

List of Tables

List of Figures

Acknowledgements

I would like to take this opportunity to thank Dr. Stephen K. O' Leary, my supervisor, for his continuing support and encouragement throughout the course of my Master's studies. Without him, this dream and ambition of my life, of completing a Master's program, could not have been fulfilled. I would also like to thank my Committee Members Dr. Wilson Eberle and Dr. Jahangir Hossain, and Dr. Yang Cao for their encouragement and support.

Sincere gratitude and thanks are also extended to my parents, Mr. Raj Kumar Salhotra and Late. Mrs.Madhurani Salhotra, my brother Mr. Nithin Kumar Salhotra, and all my family members, with whose support, I was able to come to Canada and further my education.

I would also like to thank Reddi P. Cheekoori, Vishal Pittalwar, Pramod Nakod, Hannah Anita, Kallol Mondal, Aparajitha Mondal, Erfan Baghani, Anant Parghi, Atul Polwar, Rajveer Dhillon, Jaspreet Shergill, all the friends, and my near and dear ones, for their help and support. I would also like to thank Shanon Hohle, Amanda Brobble, and all of the staff of the College of Graduate Studies, the School of Engineering, and the Centre for Scholarly Communication for their support.

Dedication

I would like to dedicate this thesis to my parents, Mr. Raj Kumar Salhotra and Late. Mrs. Madhurani Salhotra. My mother always had a dream to see me completing higher education. Unfortunately, you are not around me to see this dream coming true, but I always believe that you are with me and happy to see me fulfilling this dream. Cheers to you, MOM.

Chapter 1

Introduction

X-rays have played a major role in the field of medical diagnostics since they were first discovered in 1895. Wilhelm Rontgen, a German scientist working in his laboratory at the University of Wurzburg [1], is credited as being the first researcher to observe X-rays. He observed that phosphors, located at other points in his laboratory, glowed at the same time as high voltages were being applied across evacuated glass tubes in a darkened room. He dubbed the new kind of radiation as “X-radiation”,“X” being the unknown variable in a mathematical equation. His discovery was reported in a scientific paper, entitled “On a new kind of rays”, which was published in the journal *Science* in 1896 [2]. Despite all of the work that has been performed on understanding and characterizing these X-rays since the pioneering contribution of Rontgen, the term X-ray captured the popular imagination, and has remained in use up to the present day.

Subsequent analysis has shown that X-rays are merely a form of electromagnetic radiation, as is visible light. In Figure 1.1, an overview of the electromagnetic spectrum is provided [3]. In this figure, the various bands in the electromagnetic spectrum are depicted, the corresponding wavelengths and photon energies also being shown. While visible light has a wavelength that runs the gamut from 4000 to 7100 Å, where 1 Å $= 1 \times 10^{-10}$ m, X-rays

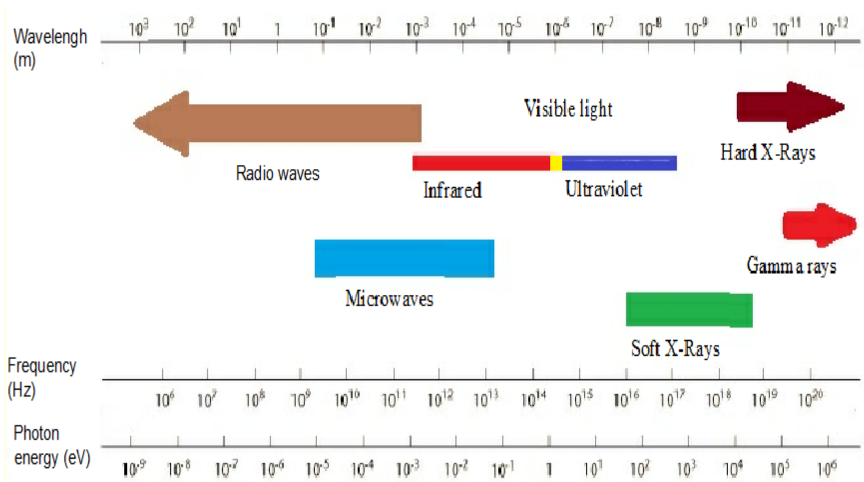

Figure 1.1: The electromagnetic spectrum. The wavelength and photon energy scales are depicted at the top and bottom of the figure, respectively. This image is after O'Leary [3].

possess wavelengths that are smaller than 100 Å. While most solid physical objects are opaque to visible light, X-rays have the ability to penetrate through solid objects. This allows one to image the internal characteristics of such objects. It is this penetrating property of X-rays that make them useful for medical imaging purposes. Indeed, shortly after Rontgen's discovery of X-rays, X-rays were starting to be deployed in medical settings. Essentially, the discovery of X-rays has allowed for the genesis of medical imaging and radiology, fields of medicine that have greatly improved life expectancy and the quality of life in the developed world.

Conventional X-ray imagers have been in use since the late 19^{th} Century. Typically, these machines are comprised of an X-ray tube, a phosphor screen, and a film cassette. The X-ray tube emits a uniform flux of X-rays, which pass through the human subject. Since dense objects will absorb more of the X-ray flux than less dense objects, bones will absorb more of the X-ray flux than the flesh. Thus, the X-ray flux that emerges from the human subject will no longer be uniform in intensity, the regions under bones having a less intense X-ray flux than those under the flesh, i.e., a shadowed X-ray flux emerges. The resultant X-ray flux then interacts with the underlying phosphor screen, which emits light with an intensity that is ideally proportional to the X-ray flux intensity received by the screen at that particular point. The light, which the phosphor screen emits, is then captured by the cassette containing the film. A negative of the X-ray image is thus captured. The image becomes permanent following processing through chemical means. The resultant image allows the medical specialist working with the machine to acquire insights into the internal workings of that particular patient. A simplified diagram, depicting the operational principles of the conventional X-ray imager, is depicted in Figure 1.2.

There are a number of shortcomings associated with the conventional X-ray imager [4]. The patients scanned through this process are exposed to a substantial X-ray flux, and this is known to pose a potential health risk. Conventional X-ray imagers are large in size, and therefore, occupy a considerable amount of space. The images that result are of limited resolution, and no further image processing may be performed following exposure and processing, i.e., no post-exposure image processing and feature enhancement may be performed. The chemical means required in order to process the films is hazardous, the materials used for such processing being difficult to handle and potentially harmful to the environment. Finally, the image that results must be stored somewhere else for subsequent retrieval, cross-referencing, and further examination. This has become a major problem for the cash-strapped health-care sector, as a visit to the medical records section of any modern hospital will attest to.

The conventional X-ray imager, of the form depicted in Figure 1.2, has been in use in medicine for more than a century now. With all of its aforementioned limitations, researchers have been exploring means of modernizing and improving the architecture of the conventional X-ray imager. This quest has been guided by a critical thought. Surely, with the abundance of technology available in the 21st Century, a device conceived of in the 19th Century, when technological options were much more limited, can be improved. As a result of these explorations, the digital X-ray imager has been conceived of and manufactured. For the last five years, the digital X-ray

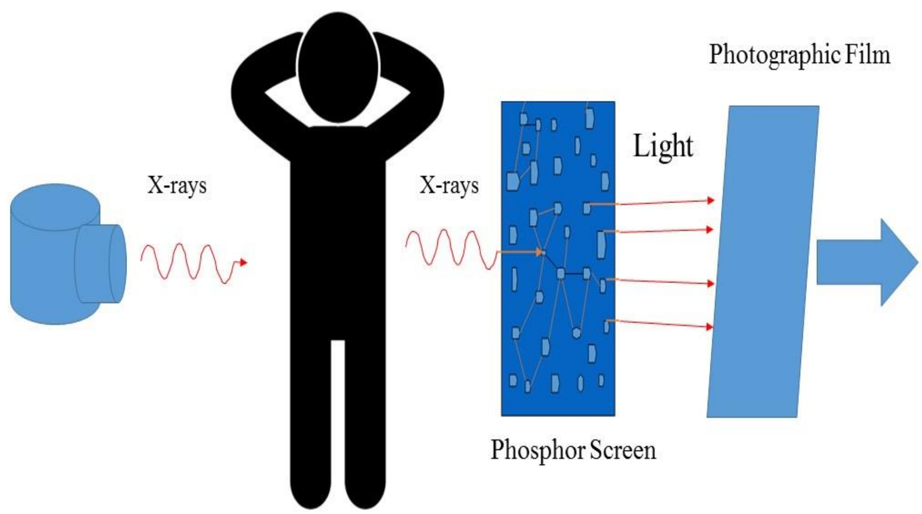

Figure 1.2: The conventional X-ray imager. This image is after O'Leary [3].

imager has started to be deployed in medical and dental clinics throughout the world, and it appears likely that most conventional X-ray imagers will be displaced by their digital counterparts within the next decade, in the developed world at least.

The digital X-ray imager performs all of the functionalities of the conventional X-ray imager, but with a substantially reduced amount of radiation dose for the same level of image quality, thereby benefiting the patient [5]. The core technology underlying the digital X-ray imager is the active matrix array, which is essentially an array of thin-film transistors upon which the rest of the imager resides. This active matrix array provides the electronic framework within which a digital X-ray image may be captured and archived. Each element of the array contains a transistor and a capacitor corresponding to an individual pixel of the X-ray image. Fundamentally, the digital X-ray imager works much like the conventional X-ray imager, i.e., a uniform X-ray flux passes through the human subject, and the emerging shadowed X-ray flux is captured by the imager. In the conventional X-ray imager, the X-ray image is captured through the use of the phosphor screen and the film cassette. In the digital X-ray imager, however, the image area is partitioned into individual pixels, and the amount of charge collected corresponding to each pixel provides a measure of the intensity of the X-ray flux corresponding to that particular pixel. Essentially, while the conventional X-ray imager captures the intensity of the light emitted off of the underlying phosphor screen, the digital X-ray imager converts the X-ray flux into a pixelated array of charges, the charge associated with each pixel being proportional to the amount of X-ray flux received by it. These charges are then stored by the capacitors associated with the different pixels. The resultant image is then read-off through the use of the peripheral electronic circuitry associated with the active matrix array. A simplified diagram of the digital X-ray imager detector is depicted in Figure 1.3 [3].

Digital X-ray imagers actually come in two distinct types: (1) direct-conversion, and (2) indirect-conversion. In the direct-conversion case, X-rays are absorbed by a photoconductor, leading to the generation of electron and hole concentrations in proportion to the incident X-ray flux intensity. That is, the absorbed X-ray flux is directly converted into charge. These charges are then collected through the application of an electric field, i.e., a voltage, on a pixel-by-pixel basis. In contrast, for the indirect-conversion case, the X-ray flux is first converted into light through the use of a scintillator, i.e., a phosphorus screen. The resultant light, emerging from the scintillator, is then detected by a pixelated array of photodiodes which converts the light intensity into electrical charges, the collected charge corresponding to each pixel ideally being proportional to the intensity of the X-ray flux received by it. In this case, the X-ray flux is indirectly converted into charge. The collected charges are then read-off through the use of the peripheral electronics, the resultant X-ray image thus being captured.

The performance of a direct-conversion digital X-ray imager is determined, in large measure, by the choice of X-ray photoconductor used within the imager. Crystalline materials, such as silicon, cannot be deposited inexpensively and uniformly over large areas, and thus, the X-ray photoconductors used within direct-conversion digital X-ray imagers are either amorphous or polycrystalline in nature. A number of materials have been

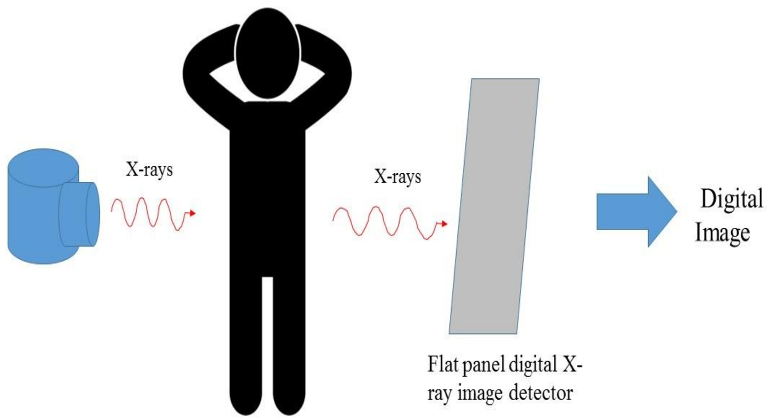

Figure 1.3: The digital X-ray imager. This image is after O'Leary [3].

considered as candidates for such photoconductive applications. Amorphous selenium (a-Se), for example, a material used in the past for xerographical purposes [6], has been identified as an excellent potential photoconductor for X-rays, i.e., a large number of electrons and holes are produced for each X-ray photon absorbed within it. At present, a-Se is being used for direct-conversion digital X-ray imagers, the resultant images being noted by medical practitioners for their exceptional quality. A number of other materials have also been considered for such applications, including cadmium zinc telluride (CdZnTe), mercury iodide (HgI_2), lead iodide (PbI_2), and thallium bromide (TlBr). To date, however, only direct-conversion digital X-ray imagers based on a-Se have actually been fabricated.

Polycrystalline and amorphous materials possess defect states which potentially can act as traps as the electrons and holes drift under the action of an applied electric field within the photoconductor. The trapping of charge within such a material leads to a reduction in the amount of collected charge received by the capacitors associated with the active matrix array following X-ray exposure. This obviously will detract from the performance of a digital X-ray imager, and understanding how the presence of such traps plays a role in shaping the performance of such detectors has become a major subject of research within this field. Through the quantitative understanding of trapping, and its role in shaping the amount of collected charge received, the performance of such a digital X-ray imager may be better understand and potentially optimized.

It is the aim of this thesis to understand how the performance of a digital X-ray imager is shaped by the particular selection of X-ray photoconductor used and then to use this understanding in order to critically evaluate the performance obtained for a number of different possible X-ray photoconductor candidates. This analysis will be cast within the framework of an elementary model for the collected charge associated with a direct-conversion digital X-ray imager. Trapping will be considered. The performance of five different X-ray photoconductors will be considered in this analysis, i.e., a-Se, CdZnTe, HgI_2, PbI_2, and TlBr. As the image intensity at a given pixel is proportional to the collected charge received by this pixel, for the purposes of this analysis, the focus will be on determining the collected charge per unit area. The collected charge attributable to the motion of the electrons and holes individually within the X-ray photoconductor, and due to the motion of both types of charges, will be considered. The sensitivity of the results to variations in the polarity of the applied voltage, and to the thickness of the photoconductor, will also be considered. Ultimately, recommendations will be made based on a critical comparison of the predicted performance for the different types of materials considered for the X-ray photoconductor.

This thesis is organized in the following manner. The background related to this work is provided in Chapter 2. Then, in Chapter 3, the properties of the different candidate X-ray photoconductors considered in this analysis are discussed, an elementary model for the performance of a direct-conversion digital X-ray imager being provided. In Chapter 4, results for the performance of the different materials considered are presented, along with comparisons between all of the materials. Finally, in Chapter 5, conclusions are drawn based on the results presented in Chapter 4.

Chapter 2

Background

2.1 Digital X-ray imagers

Digital X-ray imagers offer improved performance at reduced radiation doses, thereby benefiting the patient. They allow for all of the functionalities of the conventional X-ray imager, with a number of additional benefits. With economies of scale, their use is bound to provide cost savings for a cash-strapped sector of the economy. At present, digital X-ray imagers have been fabricated, and they are starting to be deployed in medical settings around the globe. Practising radiologists in the field are noting that the images acquired through the use of digital X-ray imagers are superior in quality to those obtained through the use of the conventional X-ray imager. With current rates of adoption, it is expected that over the next decade the digital X-ray imager will displace most conventional X-ray imagers, within the developed world at least.

In this chapter, the background related to this work is presented. First, general principles, underlying the operation of a digital X-ray imager, are presented in greater detail than that presented in Chapter 1. Then, the operational characteristics of the direct-conversion digital X-ray imager are discussed. Finally, for the sake of completeness, the operational characteristics of the indirect-conversion digital X-ray imager are featured. The discussion within this chapter will remain at a reasonably high-level. Discussions related to the subsequent technical results, and to means whereby the performance of a direct-conversion digital X-ray imager may be quantitatively evaluated, will be presented in the subsequent chapter.

This chapter is organized in the following manner. In Section 2.2, the general principles, underlying the digital X-ray imager, are discussed. Then, the operational characteristics of the direct-conversion digital X-ray imager are laid out in Section 2.3. Finally, the operational characteristics of the indirect-conversion digital X-ray imager are featured in Section 2.4.

2.2 General principles underlying the digital X-ray imager

The image captured by a digital X-ray imager is partitioned into an array of pixels, each pixel being associated with an individual element of the underlying active matrix array. The intensity of each pixel in the resultant digital X-ray image is proportional to the X-ray intensity received by that particular pixel, which in turn, should be proportional to amount of charge collected by the given pixel following X-ray exposure. These collected charges are then stored on a capacitor associated with the pixel. Following X-ray exposure, the image is then read-off, pixel-by-pixel, through the use of the peripheral electronics. The flow of charge off the capacitors during the read-off is externally orchestrated through the activation of the underlying array of thin film transistors, this array of transistors often being referred to as the active matrix array.

In the conventional X-ray imager, a phosphor screen is used in order to generate light in response to X-ray exposure. This light is then captured through the use of the accompanying film cassette. In contrast, in the digital X-ray imager, shown in Figure 2.1, the phosphor screen and film cassette of the conventional X-ray imager are reduced into a single unit which is capable of producing an X-ray image in response to a given incident X-ray flux. The associated active matrix array architecture employed for a digital X-ray imager, with individual pixels depicted, is presented in Figure 2.2.

As was mentioned in Chapter 1, the conversion of X-rays into charges may be accomplished through two distinct means: (1) direct-conversion, and (2) indirect-conversion. In direct-conversion, an X-ray photoconductor directly converts the absorbed X-ray photons into charges, i.e., electron-hole pairs. These electron-hole pairs are then collected through the application of an applied bias at the radiation receiving terminal. These collected charges reside on the capacitors associated with each pixel until read-off [7]. The amount of charge collected by each pixel is ideally proportional to the X-ray flux received by it.

2.3 The direct-conversion approach

The operating principles underlying the direct-conversion digital X-ray imager are illustrated in Figure 2.3. In this approach, an X-ray photoconductor is deposited onto an underlying active matrix array, which includes thin-film transistors, electrical leads to the peripheral electronics, the bot-

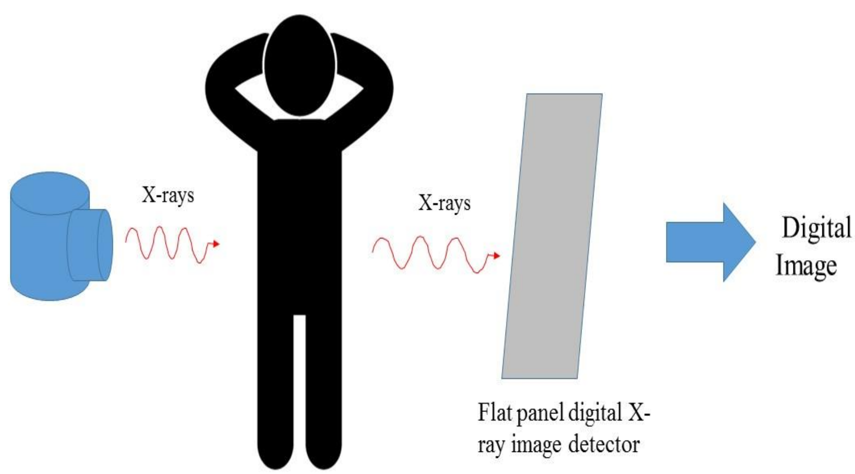

Figure 2.1: A representative digital X-ray imager. This image is after O'Leary [3].

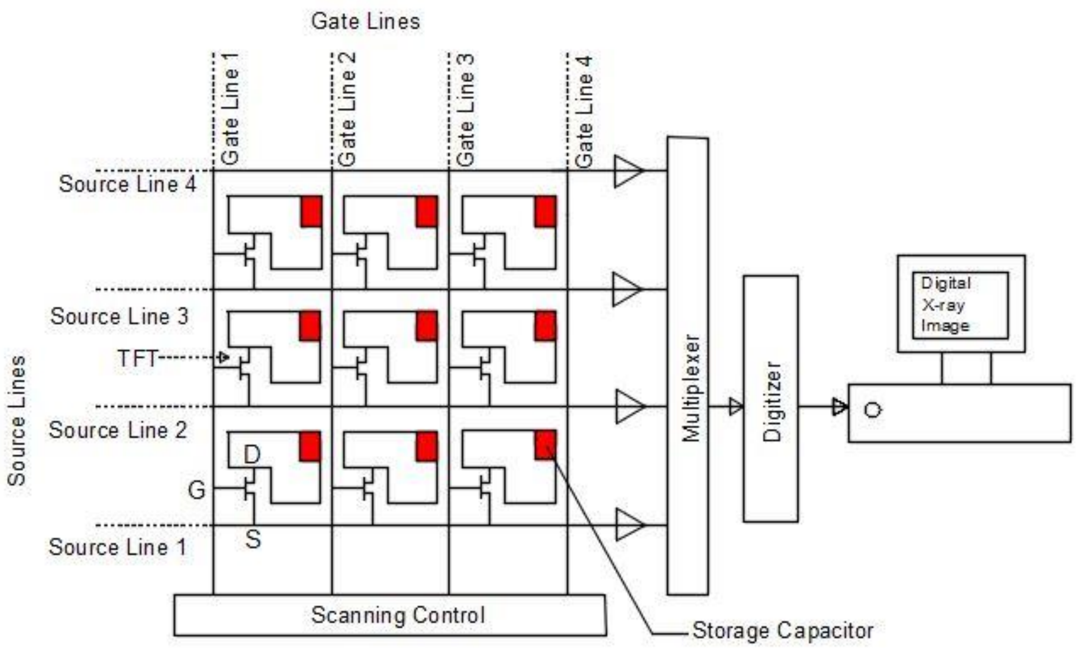

Figure 2.2: An illustration of the underlying active matrix array within a digital X-ray imager. This image is after O'Leary [3].

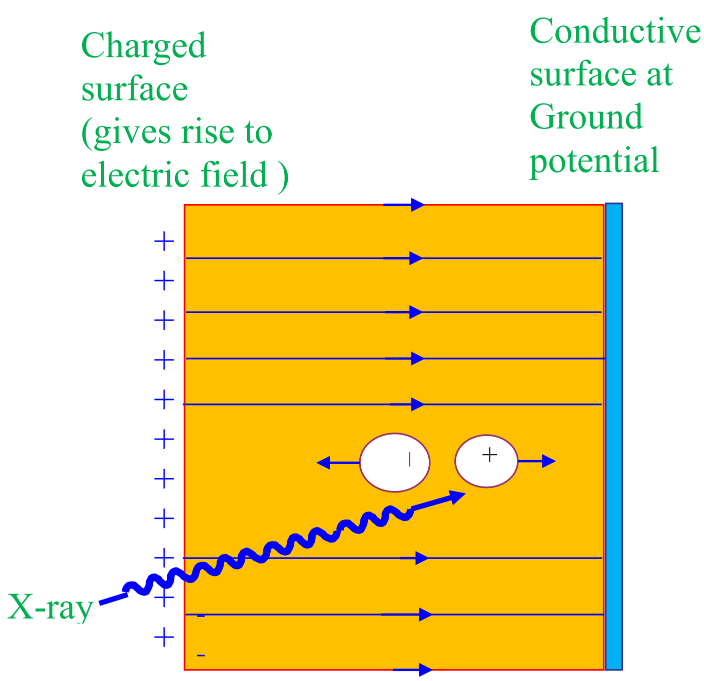

Figure 2.3: The direct-conversion approach. This image is after O'Leary [3].

tom electrode associated with each pixel, the transparent top electrode (this electrode is transparent so that very little of the X-ray flux is lost passing through it), and the associated pixel capacitor. The absorption of the X-ray photons by the photoconductor will lead to the creation of a large number of electron-hole pairs within the X-ray photoconductor, i.e., charges. As the energy associated with a given X-ray photon is orders of magnitude greater than the energy gap associated with these materials, a single absorbed X-ray photon can lead to the creation of a large number of electron-hole pairs. Through the application of a voltage to the radiation receiving top electrode, the electron-hole pairs generated within the X-ray photoconductor induce an external photocurrent, and it is this external photocurrent that generates collected charge associated with each pixel [8]. Figure 2.4 shows the process of charge collection within a single pixel. These charges are then stored by the capacitor associated with the pixel. Ultimately, the charge associated with a given pixel will be read-off through the activation of the gate associated with the thin film transistor.

At the present moment, direct-conversion digital X-ray imagers are fabricated using a-Se as the X-ray photoconductor. Familiarity with this material is the primary reason for this, i.e., a-Se has been used for a number of important applications in the past. There are, however, other types of X-ray photoconductors, including CdZnTe, HgI_2, PbI_2, and TlBr, which are also being critically evaluated for possible future use in such imagers. The aim of this thesis is to critically evaluate the performance of direct-conversion digital X-ray imagers using a variety of different X-ray photoconductors, with the hope of identifying the most promising candidate X-ray photoconductors

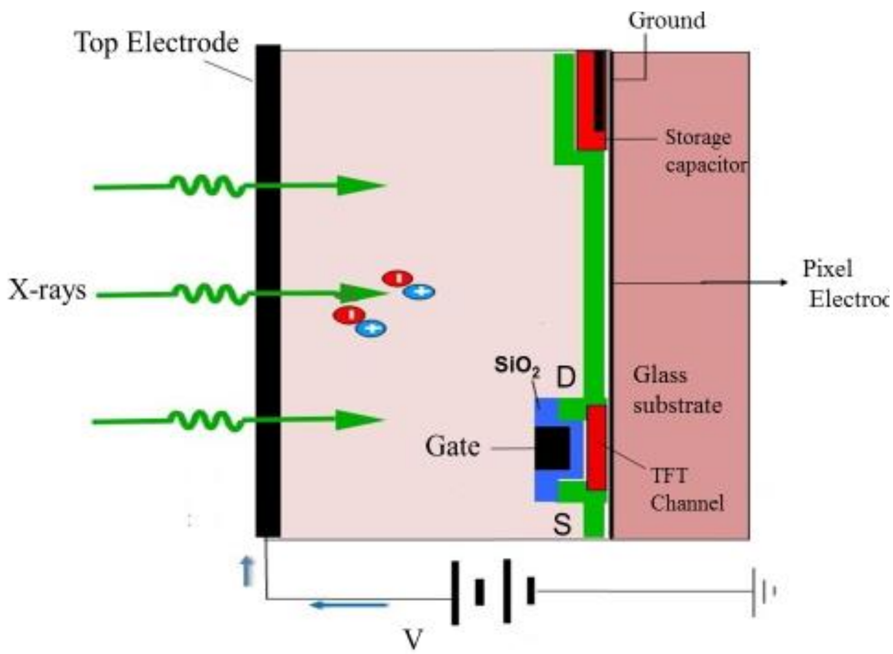

Figure 2.4: The cross-section of an individual pixel within a direct-conversion digital X-ray imager. This image is after O'Leary [3].

for such an application.

2.4 The indirect-conversion approach

The operating principles underlying the indirect-conversion digital X-ray imager are illustrated in Figure 2.5. In this approach to X-ray imaging, incident X-ray photons interact with a phosphorus screen, i.e., a scintillator, thereby producing light. The light produced by the screen is then converted into charge through an array of photodiodes, which are positioned over an underlying active matrix array of thin film transistors. The light incident to the photodiode produces charges, which are then stored on the capacitors associated with the individual pixels on the underlying active matrix array. As with the direct-conversion digital X-ray imager, these stored charges are ultimately read-off through the use of the peripheral electronics.

Unfortunately, the indirect-conversion digital X-ray imager has a fundamental limitation. In particular, the phosphor grains within the scintillator lead to light scattering. This will lead to image blurring, and ultimately limit the effectiveness of this imaging technique [4]. Thus, while indirect-conversion digital X-ray imagers are at present the dominant digital X-ray technology, the fundamental advantage offered by the direct-conversion digital X-ray imager will most likely lead to its widespread adoption in the coming years.

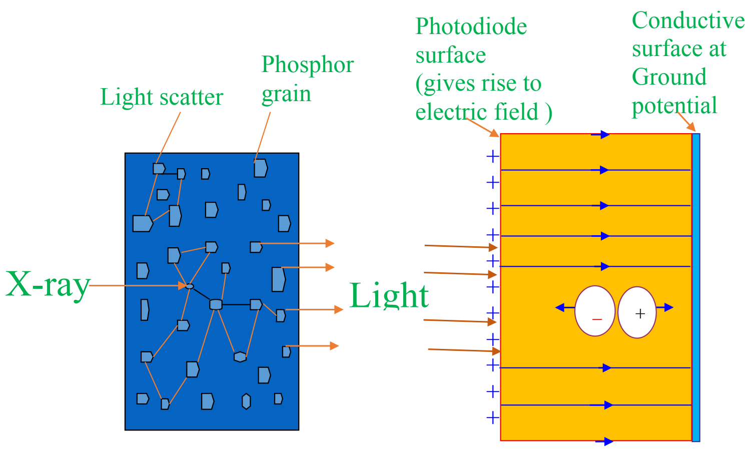

Figure 2.5: The indirect-conversion approach. This image is after O'Leary [3].

Chapter 3

Photoconductors

3.1 Scope of Analysis

Direct-conversion digital X-ray imagers offer a number of advantages when contrasted with their indirect-conversion counterparts. Within such an imager, electrons and holes are created in response to the absorption of X-ray photons. These charge are then collected on a capacitor associated with a given pixel through the application of a voltage on the radiation receiving terminal. In order to evaluate the performance of such an imager, one should have knowledge of the material properties of the X-ray photoconductors that are used within such imagers and how these material properties impact upon the corresponding device performance. This will require one to develop a relationship between the drifting charge carriers within the X-ray photoconductor and the corresponding collected charge.

It is the aim of this chapter to serve this goal. First, a detailed exposition of the ideal properties required by an X-ray photoconductor within such an imager is provided. Then each of the potential X-ray photoconductors considered, i.e., a-Se, CdZnTe, HgI_2, PbI_2, and TlBr is discussed, a tabulation of the related material properties being provided. Finally, how the drifting charges within an X-ray photoconductor relate to the corresponding collected charge is discussed, an elementary model for the charge collected from a direct-conversion digital X-ray imager being presented.

This chapter is organized in the following manner. In Section 3.2, the ideal properties of an X-ray photoconductor, for use within a direct-conversion digital X-ray imager, are presented. Then, the material properties, corresponding to the X-ray photoconductors considered in this analysis, i.e., a-Se, CdZnTe, HgI_2, PbI_2 and TlBr, are tabulated in Section 3.3. Finally, in Section 3.4, an elementary model for the performance of such a direct-conversion X-ray imager, i.e., the charge collected per unit area, is presented, this model relating the material properties and dimensions of the underlying X-ray photoconductors to the device performance. This model provides the framework for the subsequent performance analysis.

3.2 Properties of the ideal X-ray photoconductor

In order to choose which X-ray photoconductor is best suited for applications within a direct-conversion digital X-ray imager setting, a summary of the ideal X-ray photoconductor attributes provides a useful benchmark. Following the review of Kasap and Rowlands [9], a good X-ray photoconductor for such applications should possess the following properties:

- Most of the incident X-ray flux should be absorbed by the X-ray photoconductor.
- The X-ray photoconductor should produce a very large number of electron-hole pairs in response to the absorption of a single X-ray photon.

- There should be minimal bulk recombination within the X-ray photoconductor.

- There should be limited trapping of the electron-hole pairs within the X-ray photoconductor, i.e., the electrons and the holes should be transiting sufficiently fast, and the trapping should be sufficiently slow, so that very little such trapping occurs. This means that $\mu\tau F >> L$, for both the electrons and holes, where μ represents the mobility, τ represents the trapping time, F represents electric field, and L represents the thickness of the photoconductor.

- The dark current, i.e., the current that occurs without X-ray exposure, should be insignificant. That is, the contrast with the current that occurs following X-ray exposure must be significant.

- The duration of any charge carrier transit-time must be less than the pixel access time.

- The material properties should not degrade when subjected to repeated exposure to X-rays.

- The X-ray photoconductor must be easily deposited over the active matrix array.

This tabulation of ideal X-ray photoconductor properties provides a sense of the constellation of issues which the designers of a direct-conversion digital X-ray imager must deal with. In the next section, a tabulation of material properties corresponding to the X-ray photoconductors under consideration in this analysis, i.e., a-Se, CdZnTe, HgI_2, PbI_2, and TlBr is provided.

3.3 Comparison of materials properties

The coating of an X-ray photoconductor over a large area (in a microelectronics sense, surfaces of the order of 20 cm $\times$ 20 cm in dimensions are considered large areas) must be deposited using thin-film technologies. A single crystal, such as crystalline silicon, the workhorse of conventional microelectronics, can not be uniformly and inexpensively deposited over such large areas. Thus, alternate materials must be used instead for such applications. As high temperatures cannot be used for such depositions, i.e., so as not to damage the underlying active matrix array, instead polycrystalline or amorphous materials are used for such purposes. For this analysis, a number of X-ray photoconductor materials are considered, including a-Se, CdZnTe, HgI_2, PbI_2, and TlBr. Some of the basic physical properties of these materials, such as their atomic numbers, mass densities, and energy gaps, are listed in Table 3.1, and pictorially represented in Figures 3.1 and 3.2.

The performance of the digital X-ray imager critically depends on the amount of the collected charge per unit area, which itself is directly related to some of the material properties, such as the mobility-trapping-time product, i.e., $\mu\tau$. The greater the mobility-trapping-time product, the less charge trapping that occurs, and thus, the better performance of the direct-conversion digital X-ray imager. Mobility-trapping-time products for the

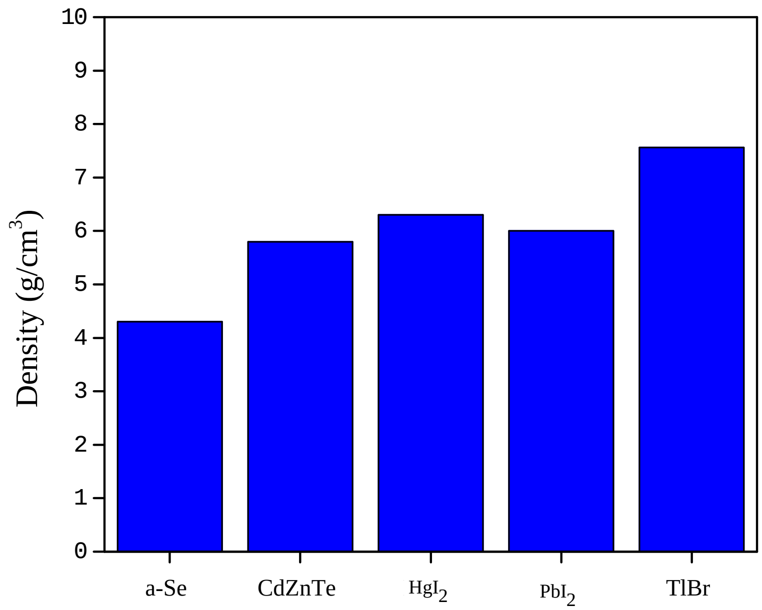

Figure 3.1: The mass density of the various X-ray photoconductors considered in this analysis. X-rays absorption is proportional to the mass density.

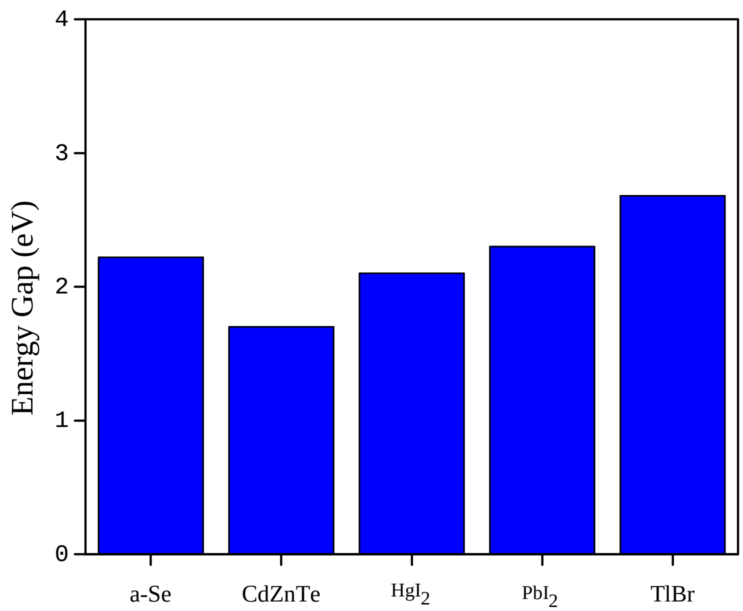

Figure 3.2: The energy gaps associated with various X-ray photoconductors considered in this analysis. Lower energy gaps favour electron-hole pair generation, i.e., there is less of a barrier.

Table 3.1: Basic physical properties of the candidate X-ray photoconductors considered in this analysis [9].

Photoconductor	Atomic numbers (Z)	Mass density (g/cm^3)	Energy gap (eV)
a-Se	Se-34	4.3	2.22
CdZnTe	Cd-48, Te-52, Zn-30	5.8	1.7
HgI_2	Hg-80, I-53	6.3	2.1
PbI_2	Pb-82, I-53	6	2.3
TlBr	Tl-81, Br-35	7.56	2.68

electrons can be represented as $\mu_e \tau_e$, while for holes it is represented as $\mu_h \tau_h$. These properties of the material, along with typical X-ray photoconductor thicknesses, the absorption linear attenuation coefficient, α, for the case of a 20 keV X-ray photon energy, and the electron-hole pair creation energy, $W_{\pm}$, are represented in Table 3.2. A comparison of the linear attenuation coefficients, α, for the X-ray photoconductors considered in this analysis, is shown in Figure 3.3. Similarly, a comparison between the mobility-trapping-time product for electrons and holes, and the electron-hole pair creation energies, $W_{\pm}$, are shown in Figures 3.4, 3.5, and 3.6, respectively. The digital X-ray imager is used for a variety of different medical applications, such as mammography, chest radiology, and fluoroscopy. Guidelines for these applications are provided in Table 3.3.

Table 3.2: Properties of the X-ray photoconductor materials considered for this analysis. 'a' is at F = 10 V/μm and 'b' is at F = 20 V/μm [8, 10–15].

X-ray photoconductor	α at 20 kev (cm^{-1})	$\mu_e\tau_e$(cm^2/V)	$\mu_h\tau_h$ (cm^2/V)	$W_\pm$ (eV)
a-Se	208.33	7.2×10^{-7}	7.0×10^{-6}	45a, 20b
CdZnTe	125	2.0×10^{-4}	3.0×10^{-6}	5
HgI_2	312.5	6.4×10^{-6}	7.0×10^{-8}	5
PbI_2	357.1	7.0×10^{-8}	2.0×10^{-6}	5
TlBr	555.5	1.7×10^{-4}	6.4×10^{-5}	6.5

Table 3.3: The applications of X-ray image detectors [10].

Clinical task	Detector size	X-ray spectrum	Mean exposure (X)
Chest radiology	32 cm$\times$43 cm	120 kVp	300 μR
Mammography	18 cm$\times$24 cm	30 kVp	12 mR
Fluroscopy	25 cm$\times$25 cm	70 kVp	1 μR

3.3.1 Amorphous Selenium (a-Se)

It is well known that a-Se may be inexpensively and uniformly deposited over large areas through the use of vacuum deposition technique [16]. The only drawback of using a-Se within direct-conversion digital X-ray imagers is its high electron-hole creation energy, $W_{\pm}$; recall Figure 3.6. For this reason, while a-Se is the only material currently in use in direct-conversion digital X-ray imager applications, other materials are being considered for use in such imagers [17].

3.3.2 Cadmium Zinc Telluride (CdZnTe)

Polycrystalline CdZnTe is fabricated using the high-pressure Bridgeman method [18]. CdZnTe is one of the most attractive materials for the direct-conversion digital X-ray imager applications owing to its high detection efficiency and energy resolution [19]. Because of its high atomic number and high mass density, more of the X-ray photons will be absorbed by this material. Unfortunately, its high leakage current and the high concentration of grain boundaries reduce the effectiveness of this material.

3.3.3 Mercury Iodide (HgI_2)

Through the use of the screen printing and physical vapor deposition, polycrystalline HgI_2 photoconductors can be easily fabricated [10]. Unfortunately, as with the case of CdZnTe, HgI_2 is characterized with high leakage currents. The particle-in-binder method can also be used to deposit a layer of HgI_2 onto the underlying active matrix array [20]. The main advantage of HgI_2 over the a-Se is its small electron-hole creation energy, $W_{\pm}$, and there-

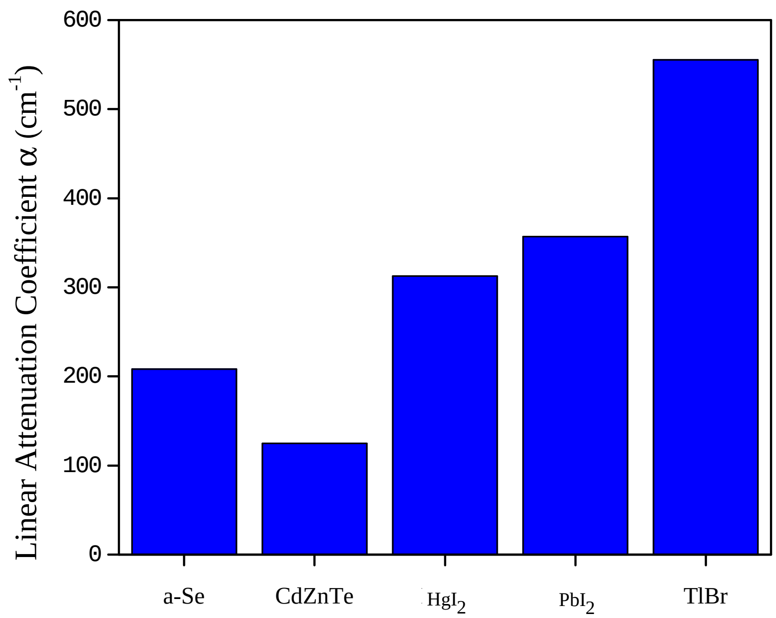

Figure 3.3: The linear attenuation coefficient, α, for the various X-ray photoconductors considered in this analysis at the X-ray photon energy of 20 KeV.

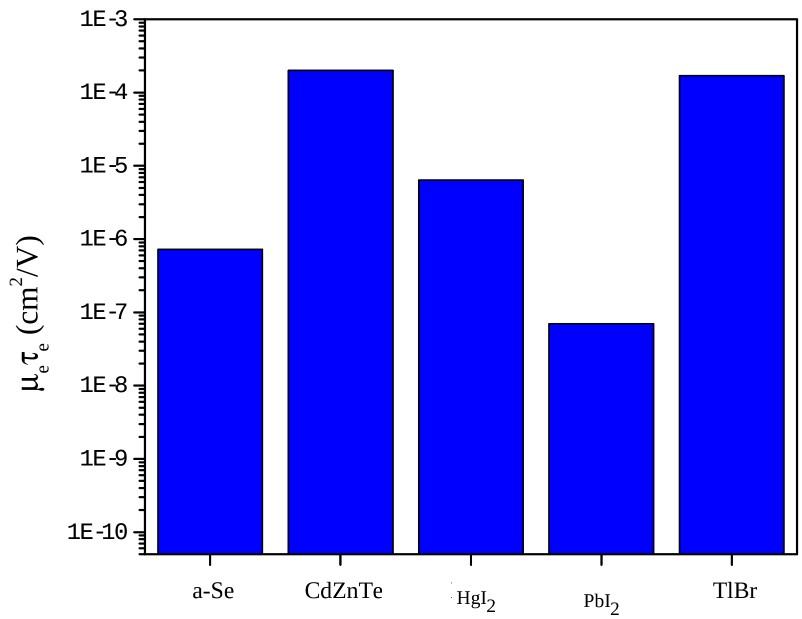

Figure 3.4: The product of the electron mobility, μ_e, and the electron trapping-time, τ_e, for the various X-ray photoconductors considered in this analysis.

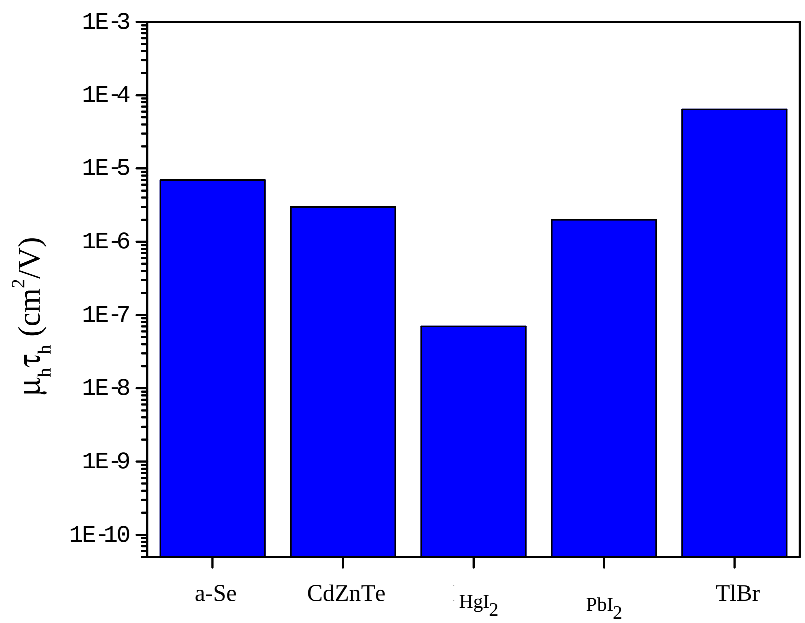

Figure 3.5: The product of the hole mobility, μ_h, and the hole trapping-time, τ_h, for various X-ray photoconductors considered in this analysis.

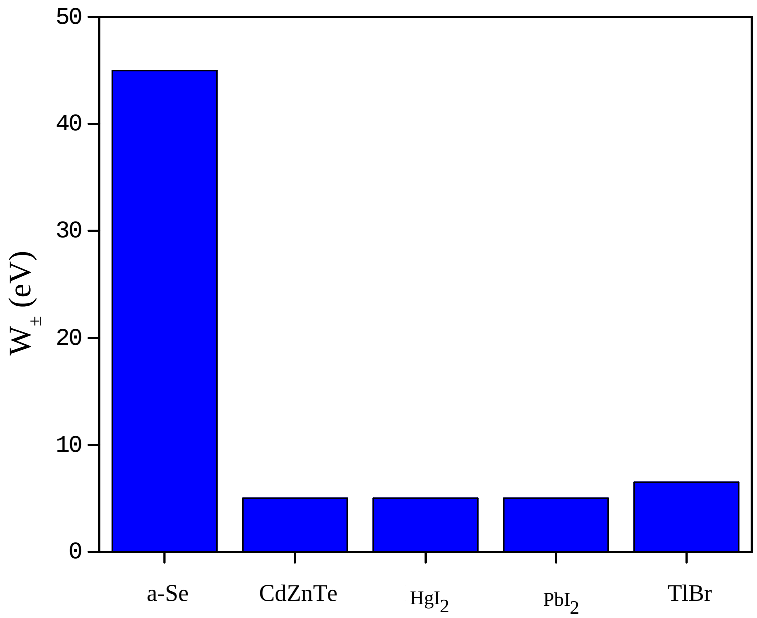

Figure 3.6: The electron-hole pair creation energy, $W_{\pm}$, for the various X-ray photoconductors considered in this analysis.

fore greater sensitivity; recall Figure 3.6. The disadvantage of HgI_2 material is its grain boundary effects [21]. This results in non-uniform surfaces and increased leakage currents.

3.3.4 Lead Iodide (PbI_2)

Polycrystalline PbI_2 goes through a process of purification before it can be used as an X-ray photoconductor. This material is typically deposited using vacuum evaporation [22]. The grain sizes of this material are smaller than those found within HgI_2. It has the additional advantage of allowing for uniform deposition. The disoriented polycrystalline structure of the material leads to high image lag, which restricts its use from certain applications in medical diagnostics, such as fluoroscopy [23].

3.3.5 Thallium Bromide (TlBr)

As with the case of PbI_2, intrinsic TlBr possesses high concentrations of impurities. Accordingly, it must be processed in order to be fit to serve as an X-ray photoconductor for applications within a direct-conversion digital X-ray imager. This processing occurs through the use of either the multipass zone refining technique or the Bridgeman-Stockbarger method, in order to limit the impact of the impurities [14]. Then the material is deposited, using technique such as thermal evaporation or the spray coating method. The advantage of this material is that it has a very large atomic number and it shows a good spectrometric performance at steady room temperature. Another feature of this material is that the electron and hole mobility-trapping-time product is quite similar, which results in uniform charge collection through the surface and also yields higher energy performance. Unfortunately, owing to grain boundary effects within the material, which results in high leakage currents, TlBr is not considered an ideal material. Because of the high leakage current, a shot noise is induced in the material, leading to a lowering of the performance of this material.

3.4 The induced external photocurrent and the resultant collected charge

The performance of a direct-conversion digital X-ray imager is determined, in large area measure, by how the drifting charges within the X-ray photoconductor induce a photocurrent in the corresponding external circuit. Accordingly, it is instructive to determine the photocurrent related to such a drifting charge within the X-ray photoconductor, under the action of an applied electric field, and the corresponding collected charge. In Figure 3.7, a representation of an electron drifting across the X-ray photoconductor, under the action of an applied electric field, and the corresponding photocurrent in the external circuit, are depicted. In this case, the radiation receiving terminal is positively biased and the electron is moving towards it. Ramo's theorem assert's that the induced photocurrent associated with the motion of this particular electron may be expressed as;

$$i_e = q\left(\frac{v_e}{L}\right), \tag{3.1}$$

where v_e denotes the electron drift velocity, q represents the electron charge, and L is the separation distance between the terminals within which the X-ray photoconductor is present, i.e., L is the X-ray photoconductor thickness.

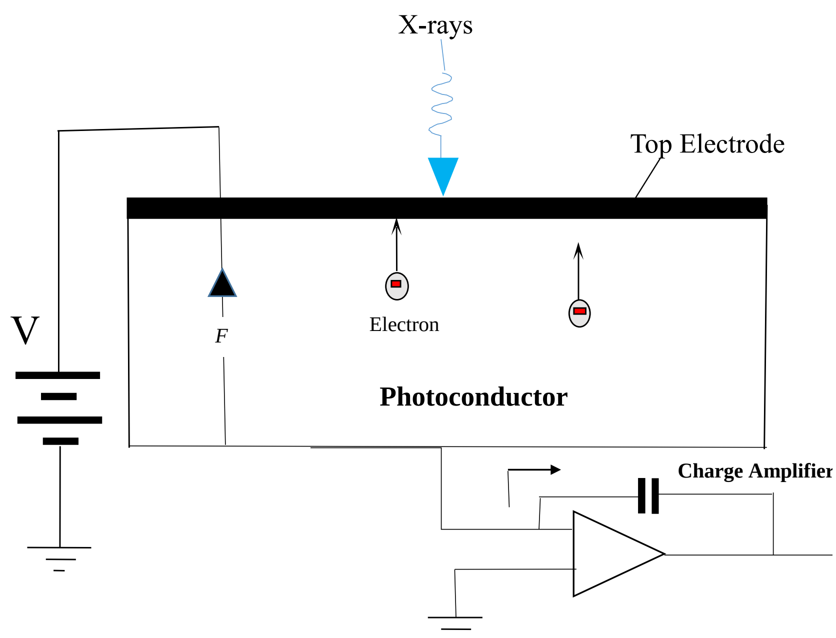

Figure 3.7: The representation of an electron drifting across the X-ray photoconductor under the action of an applied electric field. The corresponding induced photocurrent, I_{ph}, is depicted [24].

Noting that the electron will drift a distance x before reaching the radiation receiving terminal, the electron will drift for a time $\frac{x}{v_e}$. Thus, the collected charge that results from the movement of the electron from its point of origin, x, to reaching the positively biased radiation-receiving terminal,

$$q_e = q\left(\frac{x}{L}\right), \tag{3.2}$$

Similarly, for a hole, initially at x, the collected charge that results from the movement of the hole may be shown to be

$$q_h = q\left[1 - (\frac{x}{L})\right]. \tag{3.3}$$

3.5 Trapping and its role in shaping the device performance

The electrons and holes that drift across the X-ray photoconductor under the action of an applied electric field have the potential to be trapped by the traps that are present within these materials; as these are non-crystalline materials, the potential for trapping is considerable. Typically, the potential for trapping is characterized in terms of a mean trapping time, τ. Trapping clearly takes away from the possibility of an entire charge emerging from the creation of an electron and hole at a given point. The impact that trapping has on the collected charge may be characterized in terms of the Hecht relationship, i.e., the fraction of charge that is collected by the external current may be expressed as

$$\eta(\frac{x}{\mu\tau F}) = \frac{\mu\tau F}{x}\left[1 - \exp(-\frac{x}{\mu\tau F})\right] \tag{3.4}$$

where μ, τ, and F represent the drift mobility, the mean trapping-time, and the electric field, respectively, and x denotes the point where the charge was initially generated, η denotes the fraction of the charge that is collected.

The charge carrier drift velocity is the product of the drift mobility and the applied electric field strength, i.e., μF, and thus, $\mu\tau F$ correspond to the expected distance that a charge carrier, be it an electron or a hole, will drift before trapping occurs. Note that as

$$1 - z \leq \exp(-z), \tag{3.5}$$

for all z, it follows that

$$1 - \exp(-z) \leq z, \tag{3.6}$$

and therefore, for $z > 0$,

$$\frac{1 - \exp(-z)}{z} \leq 1. \tag{3.7}$$

Letting $z = \frac{x}{\mu\tau F}$, it can be shown that η in Eq. (3.4) is less than or equal to unity, i.e., $\eta \leq 1$. It is observed that in the limiting case of $\frac{x}{\mu\tau F} << 1$, i.e., when the distance from the collection terminal is less than the average trapping displacement, $\mu\tau F$, that the fraction of charge that is collected, η, as expressed in Eq. (3.4), may be reduced into a power series, i.e.,

$$\eta = \left(\frac{\mu\tau F}{x}\right)\left(1 - \left[1 - \left(\frac{x}{\mu\tau F}\right) + \frac{1}{2!}\left(\frac{x}{\mu\tau F}\right)^2 - \cdots\cdots\right]\right) \tag{3.8}$$

where the '$\cdots$' represents higher order terms. Thus, in the limit that $(\frac{x}{\mu\tau F}) \to 0$, $\eta(\frac{x}{\mu\tau F}) \to 1$. Alternatively, for $(\frac{x}{\mu\tau F}) \to \infty$, it is seen that $\eta(\frac{x}{\mu\tau F}) \to \frac{\mu\tau F}{x}$.

Using this Hecht relationship, Egs. (3.4) and (3.7) may be re-expressed as

$$q_e(x) = q\left(\frac{x}{L}\right)\eta\left(\frac{x}{\mu_e\tau_e F}\right), \tag{3.9}$$

and

$$q_h(x) = q\left[1 - \left(\frac{x}{L}\right)\right]\eta\left(\frac{L-x}{\mu_h\tau_h F}\right), \tag{3.10}$$

where the total collected charge

$$Q(x) = q_e(x) + q_h(x). \tag{3.11}$$

3.6 Performance model for a direct-conversion X-ray imager

There are number of measures available whereby the performance of a digital X-ray imager can be evaluated. The collected charge acquired per unit area following X-ray exposure is one such measure. An elementary model for the charge collected per unit area for such a digital X-ray imager is provided in the analysis of Kabir and Kasap [11]. The following assumptions underlie the analysis of Kabir and Kasap [11]

- The electric field is assumed to be uniform and constant.
- The diffusion of charge carriers is neglected.
- Each type of charge carrier is ascribed a mobility, μ, and a trapping-time, τ.
- Bulk recombination is neglected.

- The X-ray excitation pulse is treated as being instantaneous.
- Pixel differences are neglected.

The collected charge obtained per unit area may be determined through the solution of the charge continuity equation. Following the analysis of Kabir and Kasap [11], the total collected charge related to the motion of the electrons, for the case of applying a negative bias to the radiation receiving terminal, maybe shown to be:

$$Q_e = Q_o\left(\frac{\mu_e\tau_e F}{L}\right)\left((1-e^{-\alpha L}) + \frac{1}{\frac{1}{\mu_e\tau_e F}-1}\left(e^{(\frac{-L}{\mu_e\tau_e F})} - e^{-\alpha L}\right)\right), \quad (3.12)$$

where μ_e denotes the electron mobility, τ_e represents the electron trapping-time, F is the magnitude of the applied electric field, i.e., $F = V/L$, where V is the applied voltage, L is the thickness of the X-ray photoconductor, and α is the linear attenuation coefficient

$$Q_o = \frac{5.45\times 10^{13}\times eAX}{(\frac{\alpha_{air}}{\rho_{air}})W\pm}\left(\frac{\alpha_{en}}{\alpha}\right), \quad (3.13)$$

where α_{en} is the energy absorption coefficient, A is the detector area, α_{air} is the energy absorption coefficient of air, ρ_{air} is the density of air, and X is the X-ray exposure.

A similar analysis indicates that the charge related to the motion of holes for the case of applying a negative bias to the radiation receiving terminal may by shown to be expressed as

$$Q_h = Q_o\left(\frac{\mu_h\tau_h F}{L}\right)\left((1-e^{-\alpha L}) + \frac{1}{\frac{1}{\mu_h\tau_h F}-1}\left(1 - e^{-\alpha L-(\frac{L}{\mu_h\tau_h F})}\right)\right), \quad (3.14)$$

where μ_h denotes the hole mobility and τ_h represents the hole trapping-time, all other terms being define earlier. The total collected charge, Q, may be expressed as the sum of Q_e and Q_h, i.e.,

$$Q = Q_e + Q_h \tag{3.15}$$

Similarly, the total collected charge related to the motion of the electrons, for the case of applying positive bias to the radiation receiving terminal maybe shown to be:

$$Q_e = Q_o\left(\frac{\mu_e\tau_e F}{L}\right)\left(\left(1-e^{-\alpha L}\right)+\frac{1}{\frac{1}{\mu_e\tau_e F}-1}\left(1-e^{-\alpha L-(\frac{L}{\mu_e\tau_e F})}\right)\right), \tag{3.16}$$

where all the terms are defined earlier. The charge related to the motion of holes for the case of applying a positive bias to the radiation receiving terminal may by shown to be expressed as

$$Q_h = Q_o\left(\frac{\mu_h\tau_h F}{L}\right)\left(\left(1-e^{-\alpha L}\right)+\frac{1}{\frac{1}{\mu_h\tau_h F}-1}\left(e^{(\frac{-L}{\mu_h\tau_h F})}-e^{-\alpha L}\right)\right), \tag{3.17}$$

where all of the terms are defined earlier.

This elementary model for the performance of a direct-conversion digital X-ray imager, which allows for the evaluation of the collected charge per unit area in terms of a number of basic material properties, i.e., Eqs. (3.12), (3.14), and (3.15) for the case of negative bias and Eqs. (3.15), (3.16), and (3.17) for the case of positive bias, will be used in the subsequent analysis.

Chapter 4

Modeling Results

4.1 Comparative analysis

Digital X-ray imagers, capable of providing all of the functionalities of the conventional X-ray imager, but with a substantially reduced amount of radiation, are starting to be deployed in the medical sector. The direct-conversion approach to digital X-ray imaging is viewed as one of the most effective means of implementing digital X-ray imaging. In order to assess how the performance of such an imager is shaped by the X-ray photoconductor employed, the determination of the collected charge per unit area is an effective performance metric. The quality of the image depends on the amount of charge collected following X-ray exposure. A number of materials have been considered as possible materials for serving as the X-ray photoconductor within direct-conversion digital X-ray imagers, including a-Se, CdZnTe, HgI_2, PbI_2, and TlBr. A critical comparative analysis, in which the performance of these different materials, within the context of a digital X-ray imager application, is considered, is the aim of this chapter.

In this chapter, the elementary model for the performance of the direct-conversion digital X-ray imagers, introduced in the previous chapter, is used in order to form the basis of this critical comparative analysis. Five different X-ray photoconductors are considered in this analysis, namely a-Se, CdZnTe, HgI_2, PbI_2, and TlBr. For the purposes of this analysis, the collected charges, attributable to the motion of the electrons and holes individually, and due to the motion of both types of charge carriers, are considered. The voltage is applied to the radiation receiving terminal, and both positive and negative biases are considered, i.e., for the case of the positive bias, the electrons will drift towards the radiation receiving terminal and the holes will drift in the opposite direction, while for the case of the negative bias, the electrons will drift away from the radiation receiving terminal and holes will drift towards it. The fractional contributions, corresponding to the different types of charges, will also be considered. Finally, performance comparisons, corresponding to the different X-ray photoconductors considered in this analysis, will be offered. For all cases, the X-ray exposure, X, is set to 12 mR, this being the exposure corresponding to mammography; recall Table 3.3.

This chapter is organized in the following manner. Section 4.2 specifies the imager performance corresponding to the different materials which can be used as a photoconductor. A comparison of the basic material properties of the material considered is then presented in Section 4.3. Finally, results are examined and a comparison of the charge collection per unit area for the different photoconductors considered in this analysis are presented in Section 4.4.

4.2 Performance analysis

The collected charge per unit area is the performance metric that is employed for the purposes of this analysis, the performance of such an imager being tied to the amount of collected charge per unit area. The performance analysis that is performed for the different materials considered in this analysis builds upon Eqs. (3.11) and (3.12) for the case of a negative bias being applied to the radiation receiving terminal, and upon Eqs. (3.15) and (3.16) for the case of a positive bias being applied to the radiation receiving terminal. The materials considered for this analysis include a-Se, CdZnTe, HgI_2, PbI_2, and TlBr, the material parameters corresponding to these materials being drawn from Tables 3.1, 3.2 and 3.3. For each material, the contributions to the collected charge per unit area related to the motion of the electrons and holes are determined individually, as is the total collected charge due to the motion of both types of charge carriers. The dependence of the collected charge per unit area on the applied electric field and the photoconductor thickness is evaluated for the two different types of biasing conditions.

4.3 Performance for the different materials considered

4.3.1 Imager results using a-Se

In Figure 4.1, the collected charge per unit area associated with an a-Se based X-ray imager is plotted as a function of the applied electric field

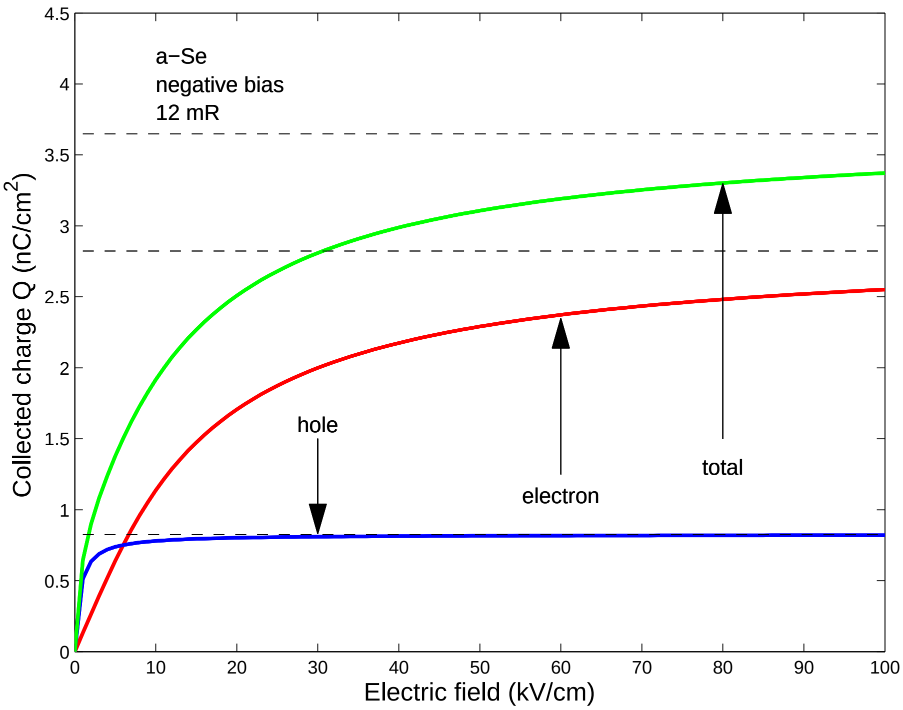

Figure 4.1: The collected charge per unit area as a function of the applied electric field strength for the case of an a-Se based X-ray imager for the imager thickness set to 200 μm for the case of negative bias. The X-ray flux, X, is set to 12 mR. The collected charge per unit area related to the motion of electrons and holes are depicted, as is the total collected charge, which of course is equal to the sum of that due to the motion of the electrons and holes. The corresponding no trapping limits, depicted with the dashed lines, are also shown. Eqs. (3.12), (3.14), and (3.15) are used to generate this plot. The online version is in color. The online version of the figure is in color.

strength for the case of the imager thickness being set to 200 μm, this result corresponding to the application of a negative bias. The collected charge per unit area related to the motion of the electrons and holes are depicted individually, as is the total collected charge per unit area. It is noted that the charge related to the motion of electrons exceeds that related to the motion of the holes by a factor of about 3.42. This might have been expected as electrons, on average, will drift longer before they reach the terminal electrode while holes drift a shorter distance; recall Ramo's theorem. It is also noted that the collected charge monotonically increases with the applied electric field strength, i.e., there are less opportunities for trapping if the charge carriers are moving faster. By taking the no-trapping limits, both associated with the motion of the electrons and the holes, upper bounds on the charge collection per unit area may be obtained, both associated with the motion of the electrons and holes, and the corresponding total collected charge. The fractional contributions to the collected charge per unit area, related to the motion of the electron and holes, corresponding to the functional dependencies depicted in Figure 4.1, are presented in Figure 4.2. As expected, the motion of electrons is the dominant contribution to the collected charge per unit area for this particular case.

In Figure 4.3, the collected charge per unit area associated with an a-Se based X-ray imager is plotted as a function of the applied electric field strength for the case of the imager thickness being set to 200 μm, this result corresponding to the application of a positive bias. The collected charge per unit area related to the motion of the electrons and holes are depicted individually, as is the total collected charge per unit area. It is noted that the

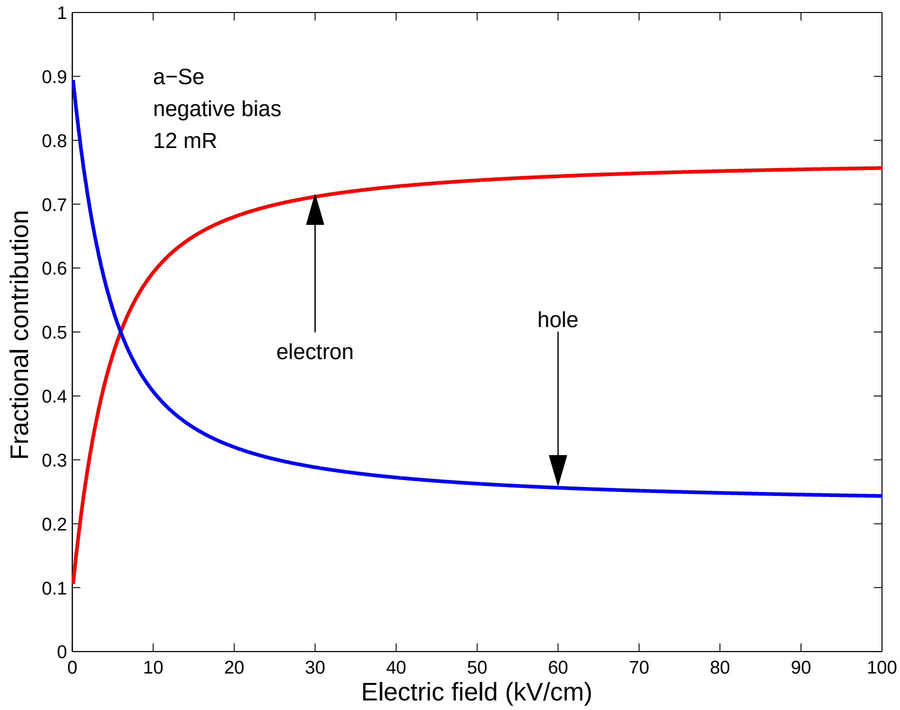

Figure 4.2: The fractional contributions to the collected charge per unit area related to the motion of the electrons and holes for an a-Se based X-ray imager for the imager thickness set to 200 μm for the case of negative bias. The X-ray flux, X, is set to 12 mR. These results are plotted as a function of the applied electric field strength. These results correspond to the results presented in Figure 4.1. Eqs. (3.12), (3.14), and (3.15) are used to generate this plot. The online version is in color.

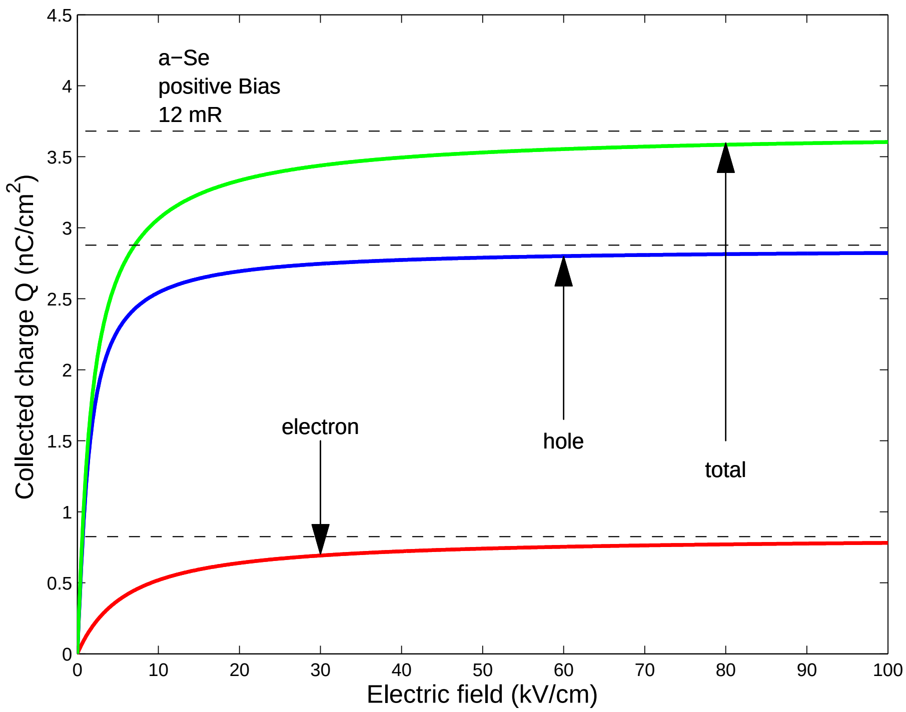

Figure 4.3: The collected charge per unit area as a function of the applied electric field strength for the case of an a-Se based X-ray imager for the imager thickness set to 200 μm for the case of positive bias. The X-ray flux, X, is set to 12 mR. The collected charge per unit area related to the motion of electrons and holes are depicted, as is the total collected charge per unit area, which of course is equal to the sum of that due to the motion of the electrons and holes. The corresponding no trapping limits, depicted with the dashed lines, are also shown. Eqs. (3.12), (3.14), and (3.15) are used to generate this plot. The online version is in color. The online version of the figure is in color.

charge related to the motion of holes exceeds that related to the motion of the electrons by a factor of about 3.479. This might have been expected as holes, on average, will drift longer before they reach the terminal electrode while electrons drift a shorter distance; recall Ramos theorem. It is also noted that the collected charge per unit area monotonically increases with the applied electric field strength, i.e., there are less opportunities for trapping if the charge carriers are moving faster. By taking the no-trapping limits, both associated with the motion of the electrons and the holes, upper bounds on the charge collection per unit area may be obtained, both associated with the motion of the electrons and holes, and the corresponding total collected charge per unit area. The fractional contributions to the collected charge per unit area, related to the motion of the electrons and holes, corresponding to the functional depenedies depicted in Figure 4.3, are presented in Figure 4.4. As expected, the motion of holes is the dominant contribution to the collected charge per unit area for this particular case.

In Figure 4.5, the collected charge per unit area associated with an a-Se based X-ray imager is plotted as a function of the imager thickness for the case of electric field strength being set to 100 kV/cm, this result corresponding to the application of a negative bias. The collected charge per unit area related to the motion of the electrons and holes are depicted individually, as is the total collected charge. It is noted that the charge per unit area related to the motion of electrons exceeds that related to the motion of the holes by a factor of about 2.773. This might have been expected as electrons, on average, will drift longer before they reach the terminal electrode while holes drift a shorter distance; recall Ramos theorem. It is also noted that

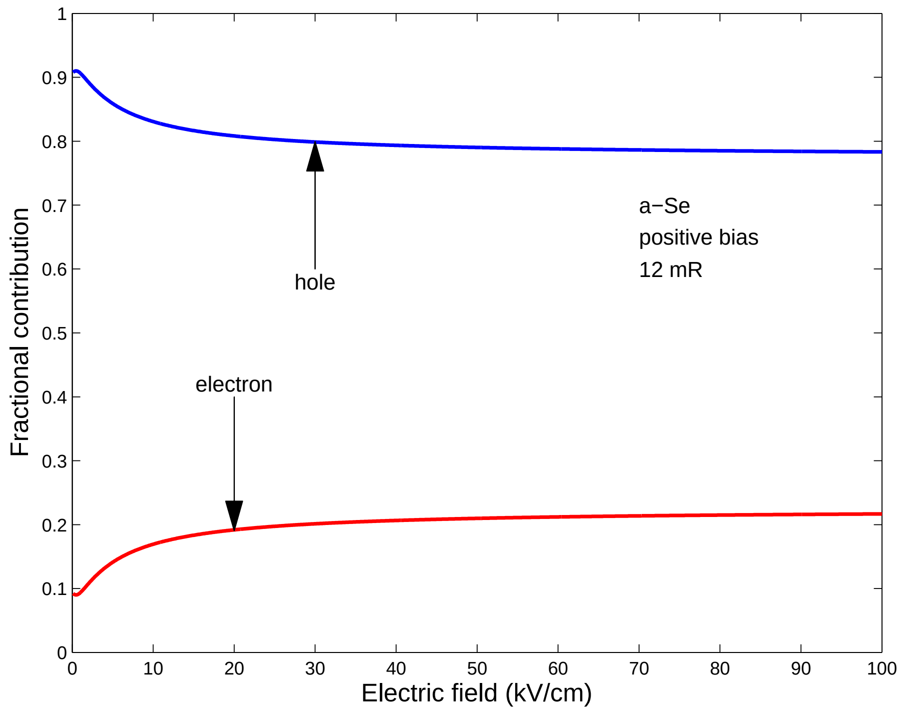

Figure 4.4: The fractional contributions to the collected charge per unit area related to the motion of the electrons and holes for an a-Se based X-ray imager for the imager thickness set to 200 μm for the case of a positive bias. The X-ray flux, X, is set to 12 mR. These results are plotted as a function of the applied electric field strength. These results correspond to the results presented in Figure 4.3. Eqs. (3.15), (3.16), and (3.17) are used to generate this plot. The online version is in color. The online version is in color.

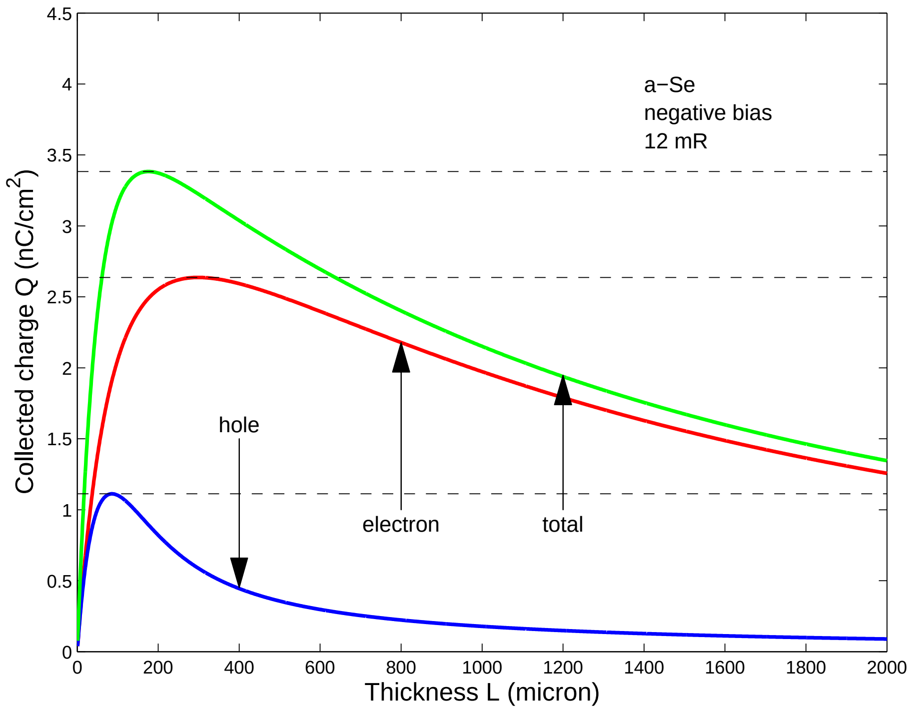

Figure 4.5: The collected charge per unit area as a function of the thickness of the X-ray imager for the case of an a-Se based X-ray imager for the electric field strength set to 100 kV/cm for the case of negative bias. The X-ray flux, X, is set to 12 mR. The collected charge per unit area related to the motion of the electrons and the holes are depicted, as is the total collected charge, which of course is equal to the sum of that due to the motion of the electrons and holes. The corresponding no trapping limits, depicted with the dashed lines, are also shown. Eqs. (3.12), (3.14), and (3.15) are used to generate this plot. The online version is in color. The online version of the figure is in color.

the amount of collected charge initially monotonically increases with the imager thickness, achieves a maximum, and then monotonically decreases in response to further increase in the X-ray imager thickness, i.e., there is an opportunity to collect a maximum amount of charge per unit area at a particular thickness of the imager. By taking the no-trapping limits, both associated with the motion of the electrons and holes, upper bounds on the charge collection per unit area may be obtained associated with the motion of the electrons and the holes, and the corresponding total collected charge per unit area. The fractional contributions to the collected charge per unit area, related to the motion of the electrons and holes, corresponding to the functional dependencies depicted in Figure 4.5, are presented in Figure 4.6. As expected, the motion of the electrons is the dominant contribution to the collected charge per unit area for this particular case.

In Figure 4.7, the collected charge per unit area associated with an a-Se based X-ray imager is plotted as a function of the X-ray imager thickness for the case of the electric field strength being set to 100 kV/cm for the case of positive bias. The collected charge per unit area related to the motion of the electrons and holes are depicted individually, as is the total collected charge. It is noted that the charge per unit area related to the motion of holes exceeds to that related to the motion of the electrons by a factor of about 5.563. This might have been expected as holes, on average, will drift longer before they reach the terminal electrode while electrons drift a shorter distance; recall Ramos theorem. It is also noted that the amount of collected charge monotonically increases with imager thickness and achieves a maximum, and then monotonically decreases in response to further increase in the thickness

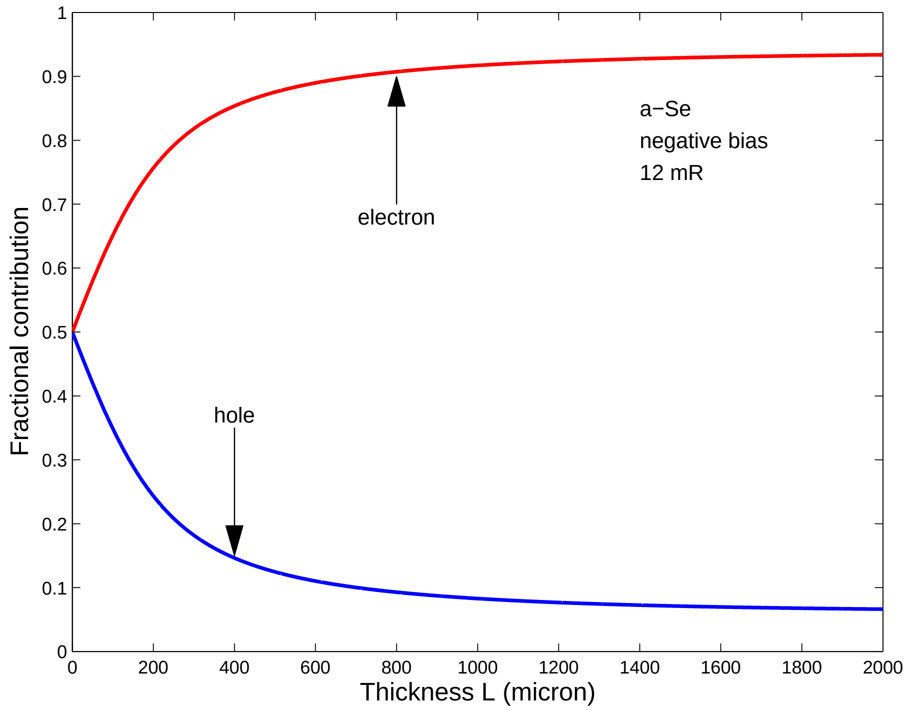

Figure 4.6: The fractional contributions to the collected charge per unit area related to the motion of the electrons and holes for an a-Se based X-ray imager for the electric field strength set to 100 kV/cm for the case of negative bias. The X-ray flux, X, is set to 12 mR. These results are plotted as a function of the imager thickness. These results correspond to the results presented in Figure 4.5. Eqs. (3.12), (3.14), and (3.15) are used to generate this plot. The online version of the figure is in color.

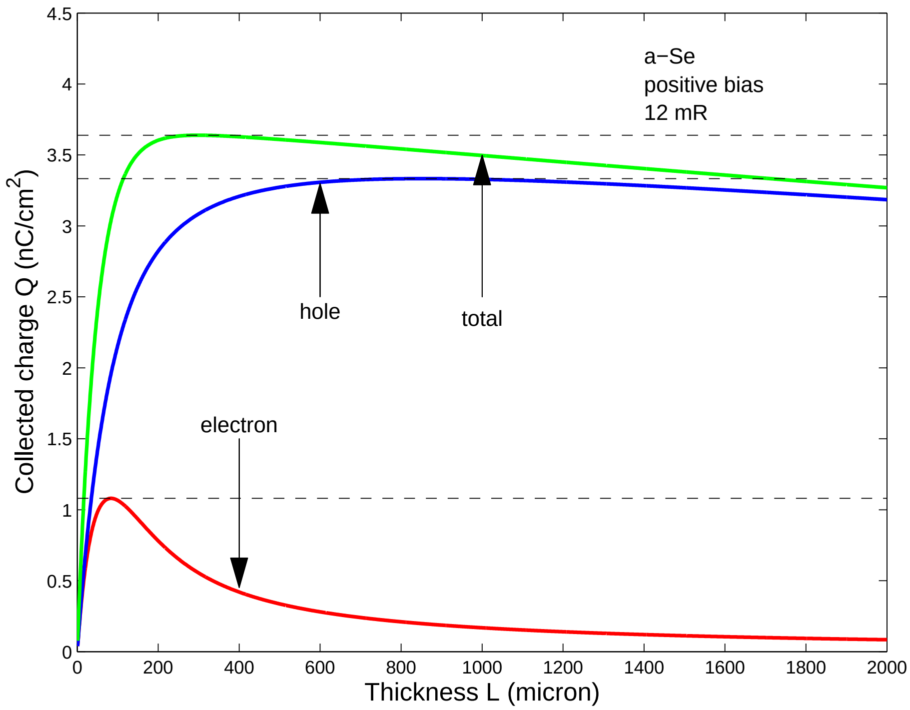

Figure 4.7: The collected charge per unit area as a function of the thickness of the X-ray imager for the case of an a-Se based X-ray imager, for the electric field strength set to 100 kV/cm for the case of positive bias. The X-ray flux, X, is set to 12 mR. The collected charge per unit area related to the motion of electrons and holes are depicted, as is the total collected charge per unit area, which of course is equal to the sum of that due to the motion of the electrons and holes. The corresponding no trapping limits, depicted with the dashed lines, are also shown. Eqs. (3.15), (3.16), and (3.17) are used to generate this plot. The online version of the figure is in color.

of the X-ray imager, i.e., there is an opportunity to collect a maximum amount of charge per unit area at a particular thickness of the X-ray imager. By taking the no-trapping limits, both associated with the motion of the electrons and holes, upper bounds on the charge collection per unit area may be obtained associated with the motion of the electrons and the holes, and the corresponding total collected charge. The fractional contributions to the collected charge per unit area related to the motion of the electrons and holes, corresponding to the functional dependence depicted in Figure 4.7, are presented in Figure 4.8. As expected, the motion of the holes is the dominant contribution to the collected charge per unit area for this particular case.

4.3.2 Imager results using CdZnTe

In Figure 4.9, the collected charge per unit area associated with a CdZnTe based X-ray imager is plotted as a function of the applied electric field strength for the case of the imager thickness being set to 2000 μm, this result corresponding to the application of a negative bias. The collected charge per unit area related to the motion of the electrons and holes are depicted individually, as is the total collected charge per unit area. It is noted that the charge related to the motion of electrons exceeds to that related to the motion of the holes by a factor of about 24.05. This might have been expected as electrons, on average, will drift longer before they reach the terminal electrode while holes drift a shorter distance; recall Ramo's theorem. It is also noted that the collected charge per unit area monotonically increases with the applied electric field strength, i.e., there are less opportunities for

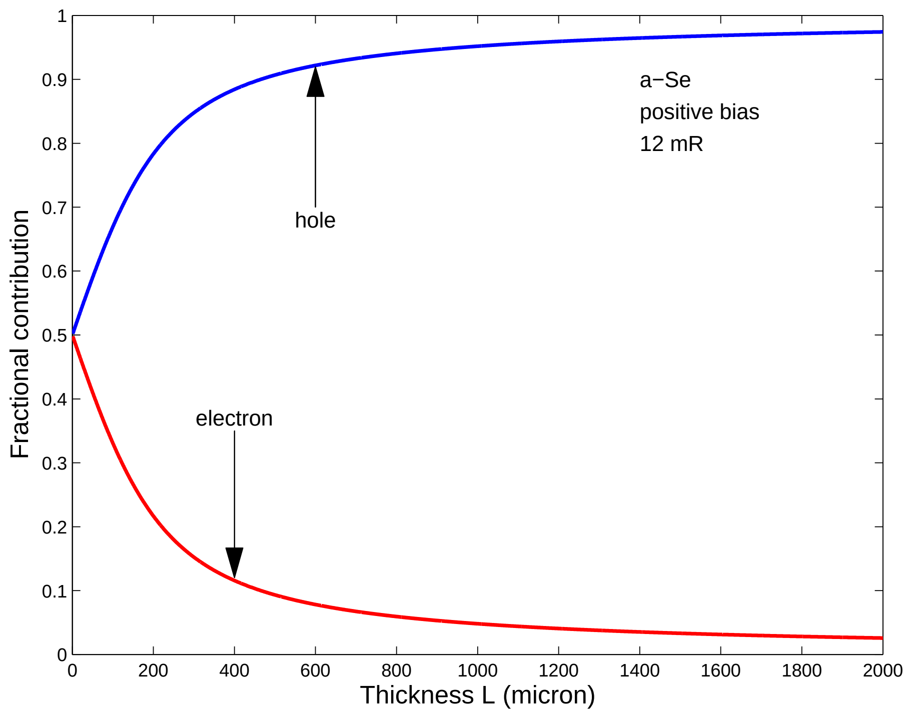

Figure 4.8: The fractional contributions to the collected charge per unit area related to the motion of the electrons and holes for an a-Se based X-ray imager for the electric field strength set to 100 kV/cm for the case of positive bias. The X-ray flux, X, is set to 12 mR. These results are plotted as a function of the X-ray imager thickness. These results correspond to the results presented in Figure 4.7. Eqs. (3.15), (3.16), and (3.17) are used to generate this plot. The online version is in color.

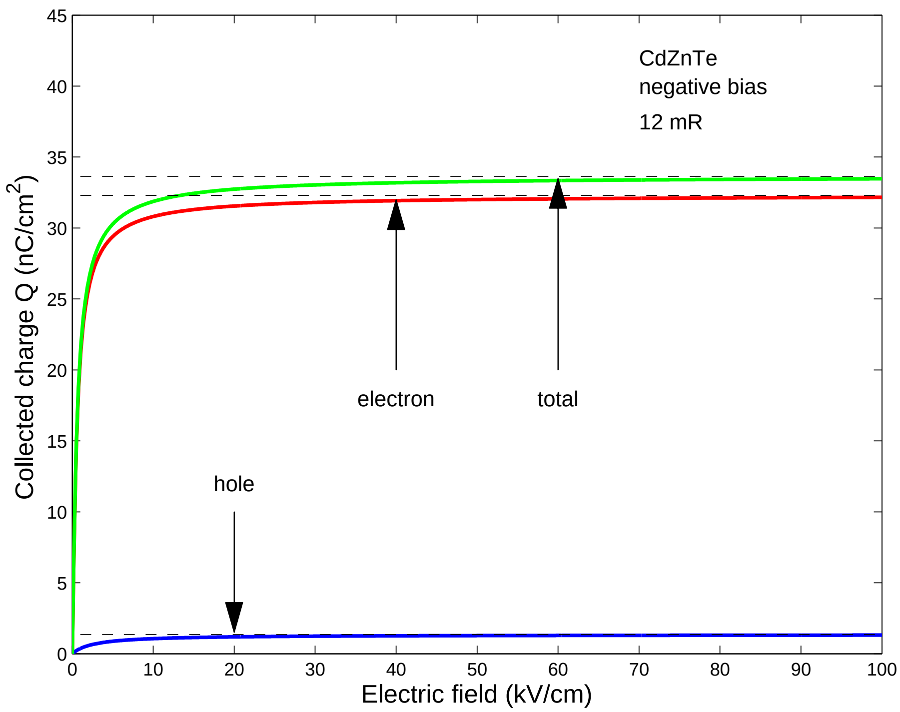

Figure 4.9: The collected charge per unit area as a function of the applied field strength for the case of a CdZnTe based X-ray imager, for the imager thickness set to 2000 μm for the case of negative bias. The X-ray flux, X, is set to 12 mR. The collected charge related to the motion of the electron and hole individually shown, as is the total charge, which of course is equal to the sum of that due to the motion of the electrons and holes. The corresponding no trapping limits, depicted with the dashed lines, are also shown. Eqs. (3.12), (3.14), and (3.15) are used to generate this plot. The online version of the figure is in color.

trapping if the charge carriers are moving faster. By taking the no-trapping limits, both associated with the motion of the electrons and the holes, upper bounds on the charge collection per unit area may be obtained, both associated with the motion of electrons and holes, and the corresponding total collected charge. The fractional contributions to the collected charge per unit area, related to the motion of the electrons and holes, corresponding to the functional dependencies depicted in Figure 4.9, are presented in Figure 4.10. As expected, the motion of electrons is the dominant contribution to the collected charge per unit area for this particular case.

In Figure 4.11, the collected charge per unit area associated with a CdZnTe based X-ray imager is plotted as a function of the applied electric field strength for the case of the imager thickness being set to 2000 μm, this result corresponding to the application of a positive bias. The collected charge per unit area related to the motion of the electrons and holes are depicted individually, as is the total collected charge. It is noted that the charge related to the motion of holes exceeds to that related to the motion of the electrons by a factor of about 23.98. This might have been expected as holes, on average, will drift longer before they reach the terminal electrode while electrons drift a shorter distance; recall Ramos theorem. It is also noted that the collected charge monotonically increases with the applied electric field strength, i.e., there are less opportunities for trapping if the charge carriers are moving faster. By taking the no-trapping limits, both associated with the motion of the electrons and the holes, upper bounds on the charge collection per unit area may be obtained, both associated with the motion of the electrons and holes, and the corresponding total collected

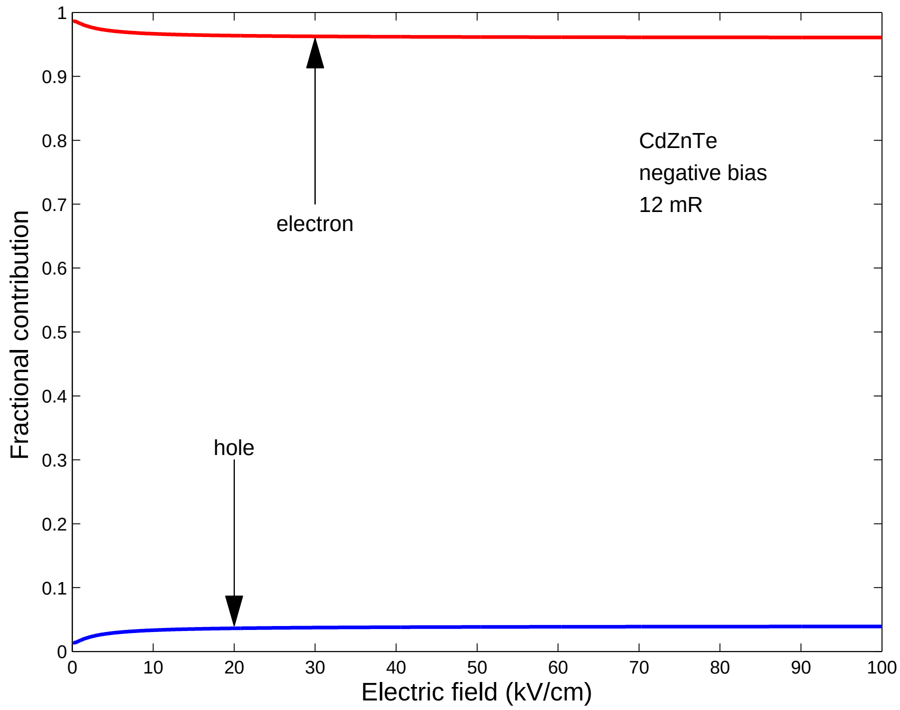

Figure 4.10: The fractional contributions to the collected charge per unit area related to the motion of the electrons and holes for a CdZnTe based X-ray imager for the imager thickness set to 2000 μm for the case of negative bias. The X-ray flux, X, is set to 12 mR. These results are plotted as a function of the applied electric field strength. These results correspond to the results presented in Figure 4.9. Eqs. (3.12), (3.14), and (3.15) are used to generate this plot. The online version is in color.

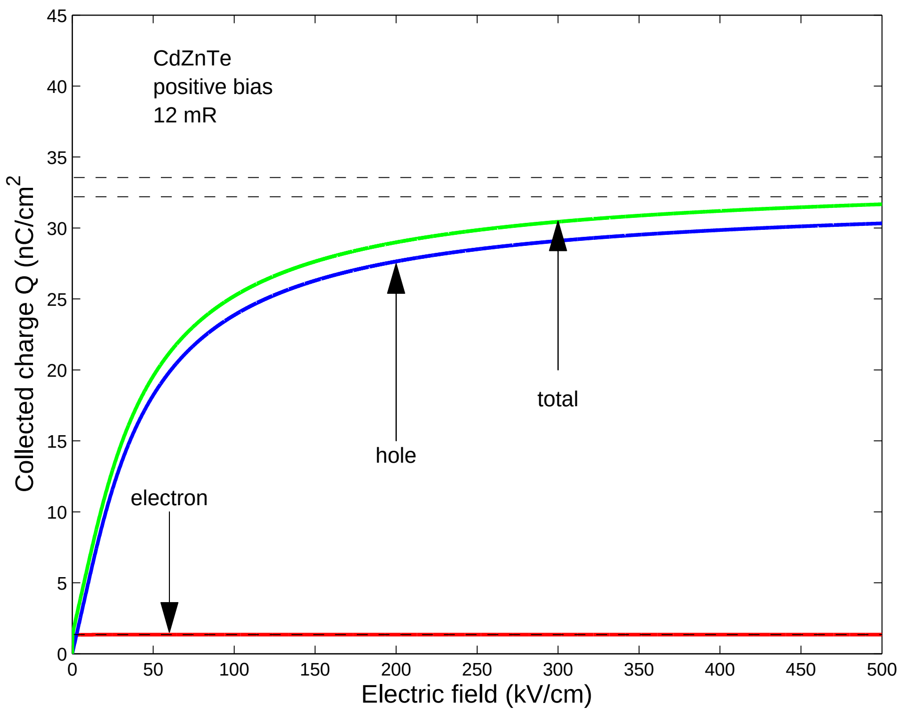

Figure 4.11: The collected charge as a function of the applied electric field strength for the case of a CdZnTe based X-ray imager for the imager thickness set to 2000 μm for the case of positive bias. The X-ray flux, X, is set to 12 mR. The collected charge per unit area related to the motion of electrons and holes are depicted, as is the total collected charge per unit area, which of course is equal to the sum of that due to the motion of the electrons and holes. The corresponding no trapping limits, depicted with the dashed lines, are also shown. Eqs. (3.15), (3.16), and (3.17) are used to generate this plot. The online version of the figure is in color.

charge per unit area. The fractional contributions to the collected charge per unit area, related to the motion of the electrons and holes, corresponding to the functional dependencies depicted in Figure 4.11, are presented in Figure 4.12. As expected, the motion of holes is the dominant contribution to the collected charge per unit area for this particular case.

In Figure 4.13, the collected charge per unit area associated with a CdZnTe based X-ray imager is plotted as a function of the imager thickness for the case of electric field strength being set to 100 kV/cm, this result corresponding to the application of a negative bias. The collected charge per unit area related to the motion of the electrons and holes are depicted individually, as is the total collected charge. It is noted that the charge related to the motion of electrons exceeds that related to the motion of the holes by a factor of about 10.503. This might have been expected as electrons, on average, will drift longer before they reach the terminal electrode while holes drift a shorter distance; recall Ramos theorem. It is also noted that the amount of collected charge initially monotonically increases with the imager thickness, achieves a maximum, and then monotonically decreases in response to further increase in the X-ray imager thickness, i.e., there is a opportunity to collect a maximum number of charge at a particular thickness of the imager. By taking the no-trapping limits, both associated with the motion of the electrons and holes, upper bounds on the charge collection per unit area may be obtained associated with the motion of the electrons and the holes, and the corresponding total collected charge per unit area. The fractional contributions to the collected charge per unit area, related to the motion of the electrons and holes, corresponding to the functional depen-

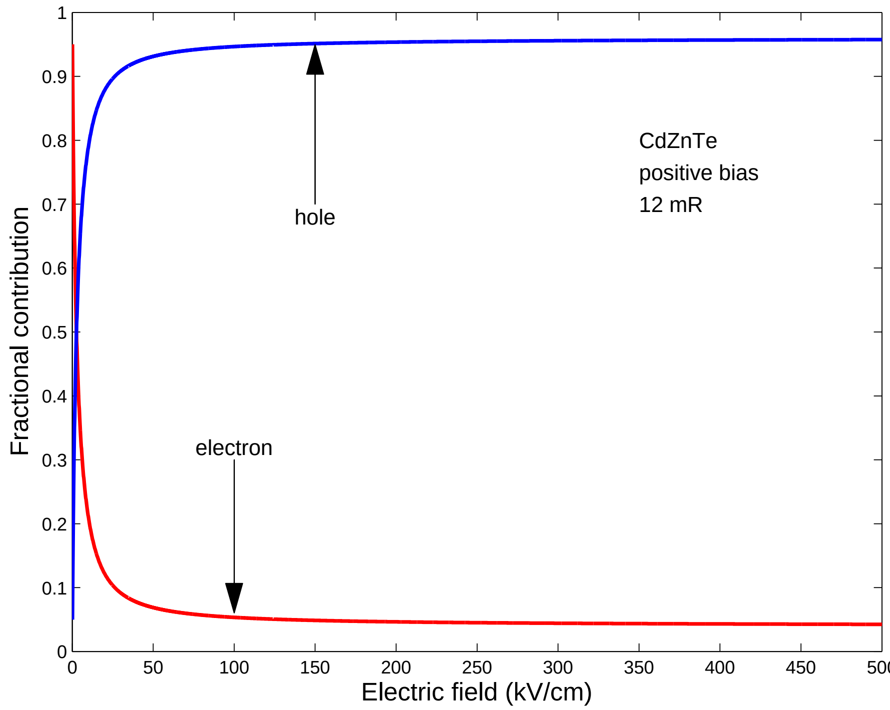

Figure 4.12: The fractional contributions to the collected charge per unit area related to the motion of the electrons and holes for a CdZnTe based X-ray imager for the imager thickness set to 2000 μm for the case of a positive bias. The X-ray flux, X, is set to 12 mR. These results are plotted as a function of the applied electric field strength. These results correspond to the results presented in Figure 4.11. Eqs. (3.15), (3.16), and (3.17) are used to generate this plot. The online version is in color.

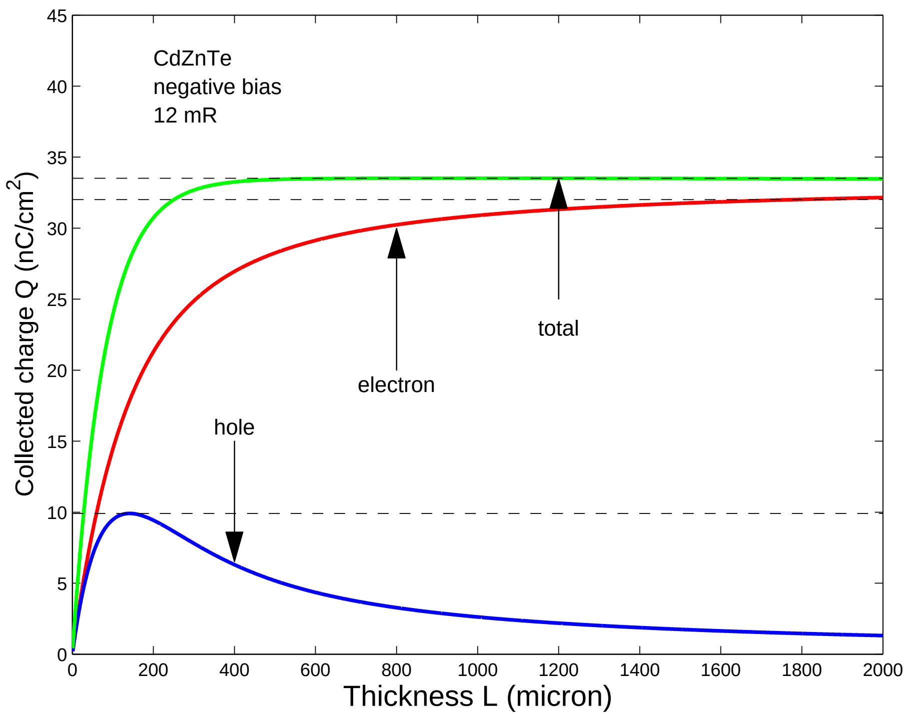

Figure 4.13: The collected charge per unit area as a function of the thickness of the X-ray imager for the case of a CdZnTe based X-ray imager for the electric field strength set to 100 kV/cm for the case of negative bias. The X-ray flux, X, is set to 12 mR. The collected charge related to the motion of the electrons and the holes are depicted, as is the total collected charge, which of course is equal to the sum of that due to the motion of the electrons and holes. The corresponding no trapping limits, depicted with the dashed lines, are also shown. Eqs. (3.12), (3.14), and (3.15) are used to generate this plot. The online version of the figure is in color.

dence depicted in Figure 4.13, are presented in Figure 4.14. As expected, the motion of the electrons is the dominant contribution to the collected charge per unit area for this particular case.

In Figure 4.15, the collected charge per unit area associated with a CdZnTe based X-ray imager is plotted as a function of the X-ray imager thickness for the case of the electric field strength being set to 100 kV/cm for the case of positive bias. The collected charge per unit area related to the motion of the electrons and holes are depicted individually, as is the total collected charge. It is noted that the charge related to the motion of holes exceeds to that related to the motion of the electrons by a factor of about 3.559. This might have been expected as holes, on average, will drift longer before they reach the terminal electrode while electrons drift a shorter distance; recall Ramos theorem. It is also noted that the amount of collected charge per unit area monotonically increases with imager thickness and achieves a maximum, and then monotonically decreases in response to further increase in the thickness of the X-ray imager, i.e., there is an opportunity to collect a maximum amount of charge per unit area at a particular thickness of the X-ray imager. By taking the no-trapping limits, both associated with the motion of the electrons and holes, upper bounds on the charge collection per unit area may be obtained associated with the motion of the electrons and holes, and the corresponding total collected charge. The fractional contributions to the collected charge per unit area related to the motion of the electrons and holes, corresponding to the functional dependence depicted in Figure 4.15, are presented in Figure 4.16. As expected, the motion of the holes is the dominant contribution to the collected charge

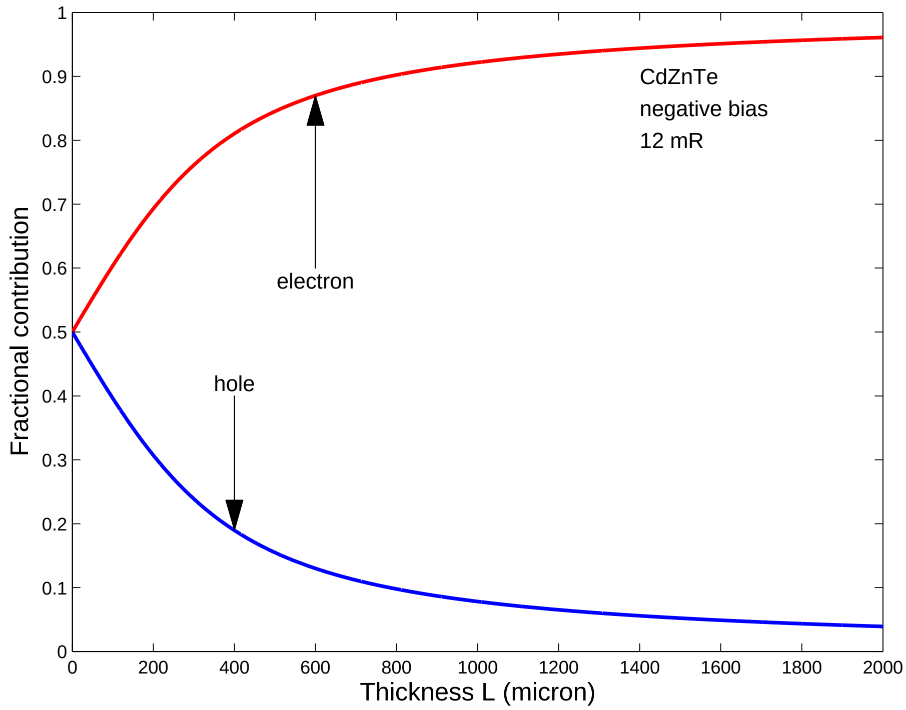

Figure 4.14: The fractional contributions to the collected charge per unit area related to the motion of the electrons and holes for a CdZnTe based X-ray imager for the electric field strength set to 100 kV/cm for the case of negative bias. The X-ray flux, X, is set to 12 mR. These results are plotted as a function of the imager thickness. These results correspond to the results presented in Figure 4.13. Eqs. (3.12), (3.14), and (3.15) are used to generate this plot. The online version of the figure is in color.

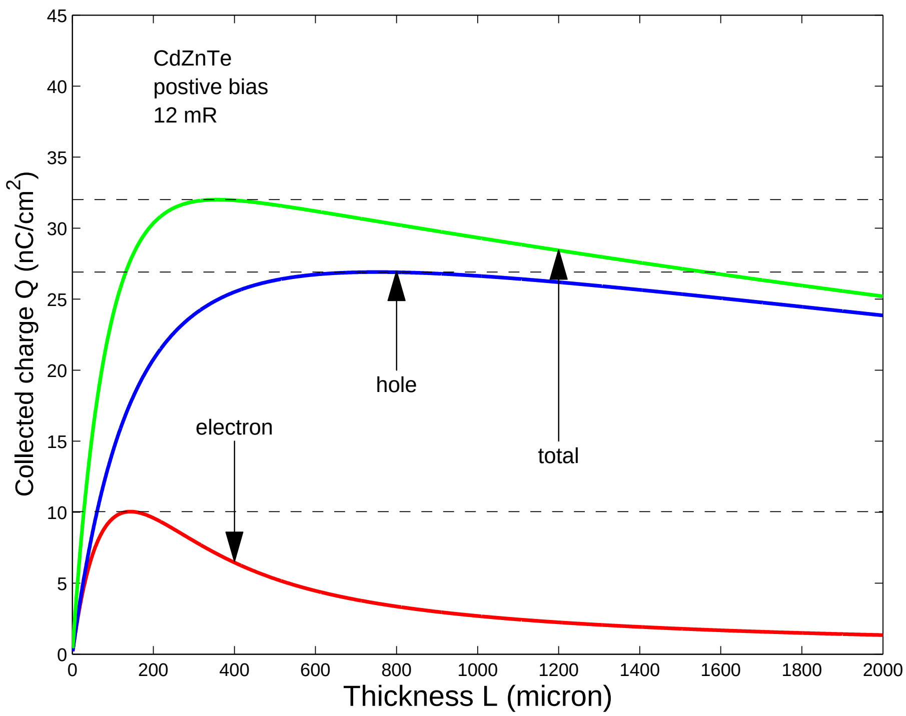

Figure 4.15: The collected charge per unit area as a function of the thickness of the X-ray imager for the case of a CdZnTe based X-ray imager, for the electric field strength set to 100 kV/cm for the case of positive bias. The X-ray flux, X, is set to 12 mR. The collected charge per unit area related to the motion of electrons and holes are depicted, as is the total collected charge, which of-course is equal to the sum of that due to the motion of the electrons and holes. The corresponding no trapping limits, depicted with the dashed lines, are also shown. Eqs. (3.15), (3.16), and (3.17) are used to generate this plot. The online version of the figure is in color.

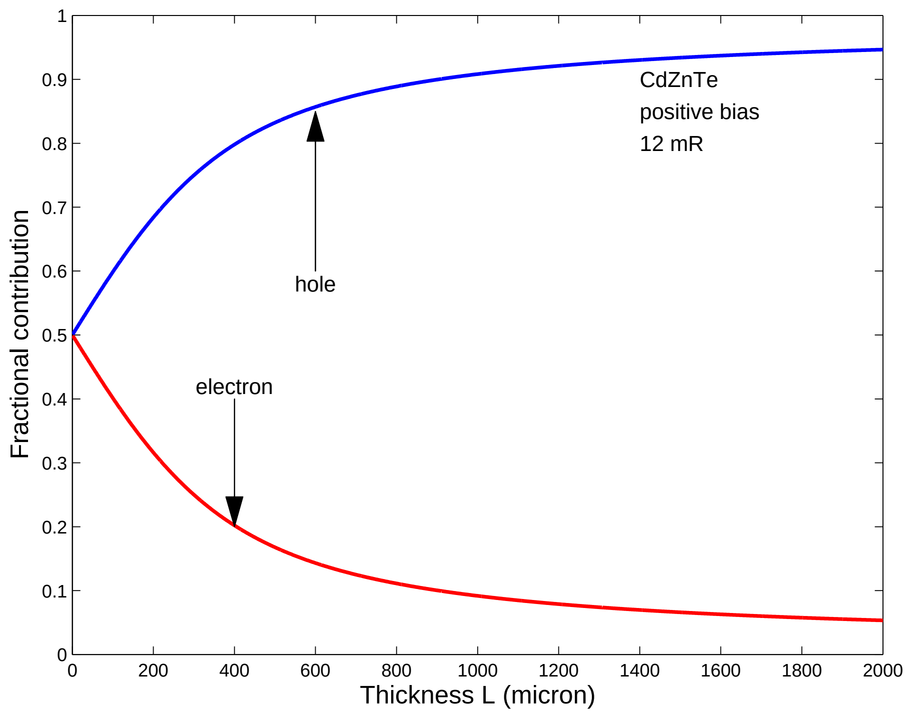

Figure 4.16: The fractional contributions to the collected charge per unit area related to the motion of the electrons and holes for a CdZnTe based X-ray imager for the electric field strength set to 100 kV/cm for the case of positive bias. The X-ray flux, X, is set to 12 mR. These results are plotted as a function of the imager thickness. These results correspond to the results presented in Figure 4.15. Eqs. (3.15), (3.16), and (3.17) are used to generate this plot. The online version of the figure is in color.

per unit area for this particular case.

4.3.3 Imager results using HgI_2

In Figure 4.17, the collected charge per unit area associated with a HgI_2 based X-ray imager is plotted as a function of the applied electric field strength for the case of the imager thickness being set to 250 μm, this result corresponding to the application of a negative bias. The collected charge per unit area related to the motion of the electrons and holes are depicted individually, as is the total collected charge. It is noted that the charge related to the motion of electrons exceeds to that related to the motion of the holes by a factor of about 6.8668. This might have been expected as electrons, on average, will drift longer before they reach the terminal electrode while holes drift a shorter distance; recall Ramo's theorem. It is also noted that the collected charge monotonically increases with the applied electric field strength, i.e., there are less opportunities for trapping if the charge carriers are moving faster. By taking the no-trapping limits, both associated with the motion of the electrons and the holes, upper bounds on the charge collection per unit area may be obtained, both associated with the motion of electrons and holes, and the corresponding total collected charge. The fractional contributions to the collected charge per unit area, related to the motion of the electrons and holes, corresponding to the functional dependencies depicted in Figure 4.17, are presented in Figure 4.18. As expected, the motion of electrons is the dominant contribution to the collected charge per unit area for this particular case.

In Figure 4.19, the collected charge per unit area associated with a HgI_2

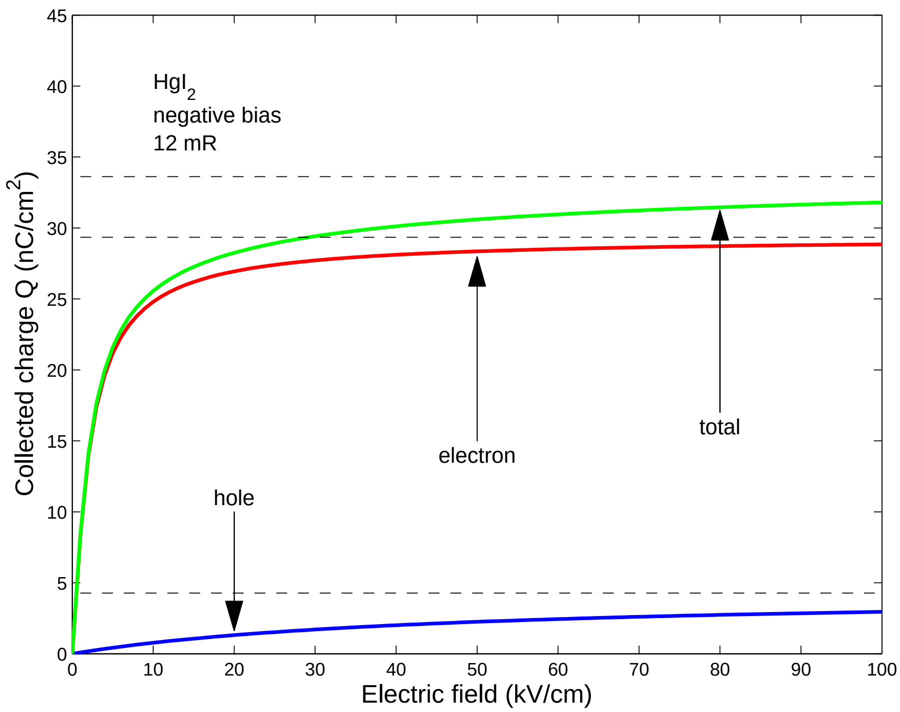

Figure 4.17: The collected charge per unit area as a function of the applied electric field strength for the case of a HgI_2 based X-ray imager for the imager thickness set to 250 μm for the case of negative bias. The X-ray flux, X, is set to 12 mR. The collected charge related to the motion of electrons and holes are depicted, as is the total collected charge, which of course is equal to the sum of that due to the motion of the electrons and holes. The corresponding no trapping limits, depicted with the dashed lines, are also shown. Eqs. (3.12), (3.14), and (3.15) are used to generate this plot. The online version of the figure is in color.

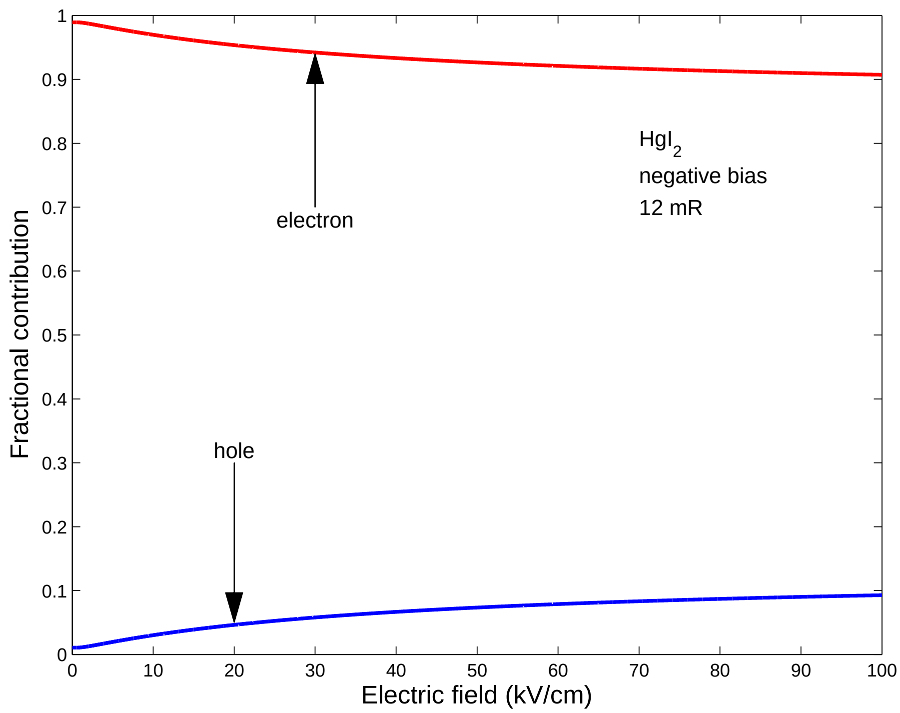

Figure 4.18: The fractional contributions to the collected charge per unit area related to the motion of the electrons and holes for a HgI_2 based X-ray imager for the imager thickness set to 250 μm for the case of negative bias. The X-ray flux, X, is set to 12 mR. These results are plotted as a function of the applied electric field strength. These results correspond to the results presented in Figure 4.17. Eqs. (3.12), (3.14), and (3.15) are used to generate this plot. The online version is in color.

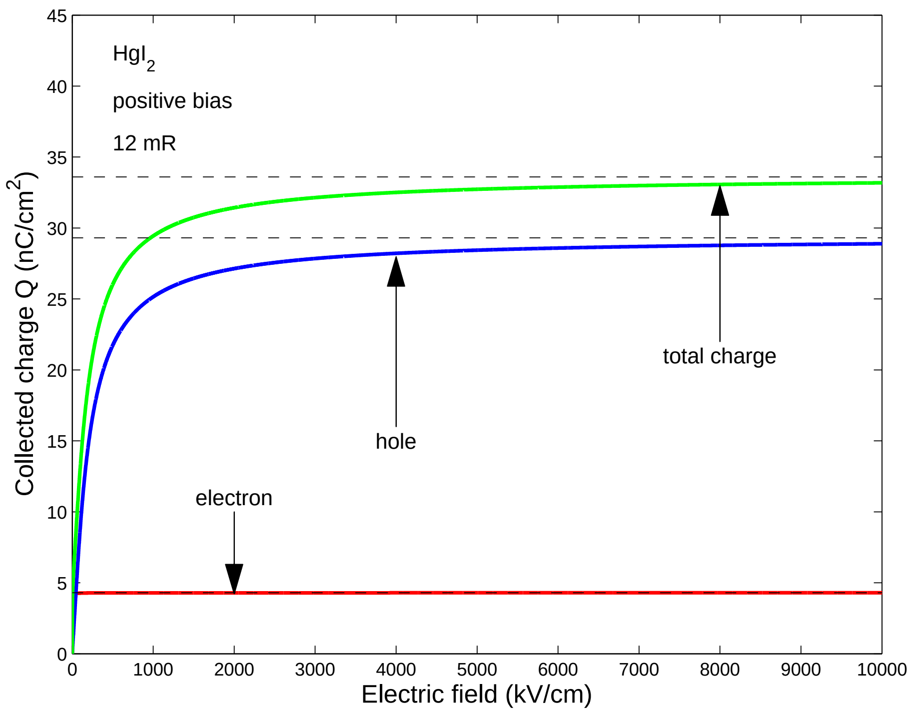

Figure 4.19: The collected charge per unit area as a function of the applied electric field strength for the case of a HgI_2 based X-ray imager for the imager thickness set to 250 μm for the case of positive bias. The X-ray flux, X, is set to 12 mR. The collected charge per unit area related to the motion of electrons and holes are depicted, as is the total collected charge, which of course is equal to the sum of that due to the motion of the electrons and holes. The corresponding no trapping limits, depicted with the dashed lines, are also shown. Eqs. (3.15), (3.16), and (3.17) are used to generate this plot. The online version of the figure is in color.

based X-ray imager is plotted as a function of the applied electric field strength for the case of the imager thickness being set to 250 μm, this result corresponding to the application of a positive bias. The collected charge related to the motion of the electrons and holes are depicted individually, as is the total collected charge. It is noted that the charge related to the motion of holes exceeds to that related to the motion of the electrons by a factor of about 6.8265. This might have been expected as holes, on average, will drift longer before they reach the terminal electrode while electrons drift a shorter distance; recall Ramos theorem. It is also noted that the collected charge monotonically increases with the applied electric field strength, i.e., there are less opportunities for trapping if the charge carriers are moving faster. By taking the no-trapping limits, both associated with the motion of the electrons and the holes, upper bounds on the charge collection per unit area may be obtained, both associated with the motion of the electrons and holes, and the corresponding total collected charge per unit area. The fractional contributions to the collected charge per unit area, related to the motion of the electrons and holes, corresponding to the functional dependencies depicted in Figure 4.19, are presented in Figure 4.20. As expected, the motion of holes is the dominant contribution to the collected charge per unit area for this particular case.

In Figure 4.21, the collected charge per unit area associated with a HgI_2 based X-ray imager is plotted as a function of the imager thickness for the case of electric field strength being set to 100 kV/cm, this result corresponding to the application of a negative bias. The collected charge per unit area related to the motion of the electrons and holes are depicted individually,

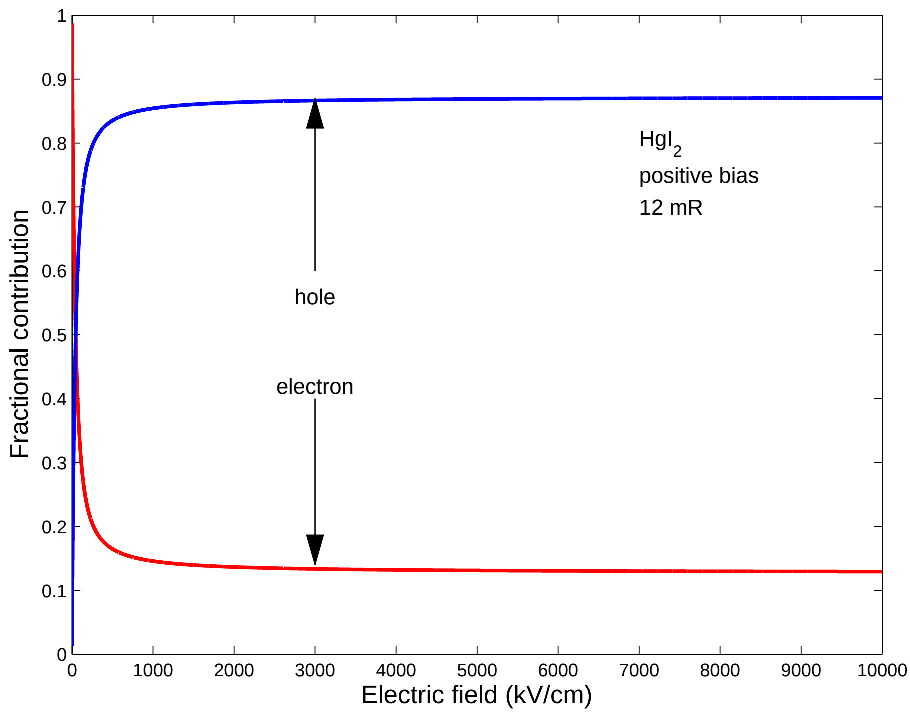

Figure 4.20: The fractional contributions to the collected charge per unit area related to the motion of the electrons and holes for a HgI_2 based X-ray imager for the imager thickness set to 250 μm for the case of a positive bias. The X-ray flux, X, is set to 12 mR. These results are plotted as a function of the applied electric field strength. These results correspond to the results presented in Figure 4.19. Eqs. (3.15), (3.16), and (3.17) are used to generate this plot. The online version is in color.

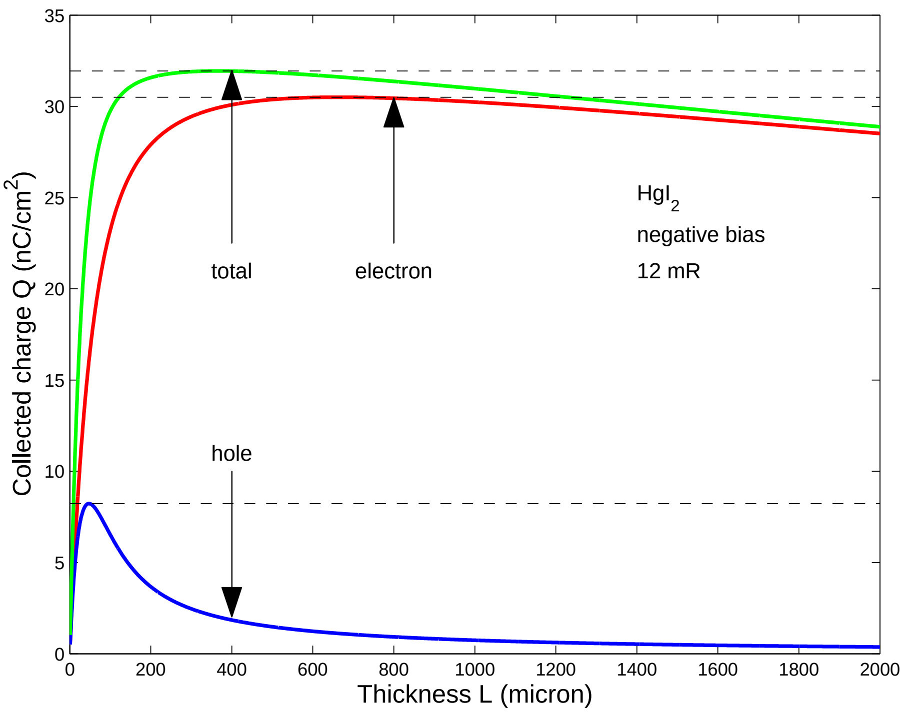

Figure 4.21: The collected charge per unit area as a function of the thickness of the X-ray imager for the case of a HgI_2 based X-ray imager for the electric field strength set to 100 kV/cm for the case of negative bias. The X-ray flux, X, is set to 12 mR. The collected charge related to the motion of the electrons and the holes are depicted, as is the total collected charge, which of course is equal to the sum of that due to the motion of the electrons and holes. The corresponding no trapping limits, depicted with the dashed lines, are also shown. Eqs. (3.12), (3.14), and (3.15) are used to generate this plot. The online version of the figure is in color.

as is the total collected charge. It is noted that the charge related to the motion of electrons exceeds that related to the motion of the holes by a factor of about 14.98. This might have been expected as electrons, on average, will drift longer before they reach the terminal electrode while holes drift a shorter distance; recall Ramos theorem. It is also noted that the amount of collected charge initially monotonically increases with the imager thickness, achieves a maximum, and then monotonically decreases in response to further increase in the X-ray imager thickness, i.e., there is a opportunity to collect a maximum number of charge at a particular thickness of the imager. By taking the no-trapping limits, both associated with the motion of the electrons and holes, upper bounds on the charge collection per unit area may be obtained associated with the motion of the electrons and the holes, and the corresponding total collected charge. The fractional contributions to the collected charge per unit area, related to the motion of the electrons and holes, corresponding to the functional dependencies depicted in Figure 4.21, are presented in Figure 4.22 . As expected, the motion of the electrons is the dominant contribution to the collected charge for this particular case.

In Figure 4.23, the collected charge per unit area associated with a HgI_2 based X-ray imager is plotted as a function of the X-ray imager thickness for the case of the electric field strength being set to 100 kV/cm for the case of positive bias. The collected charge related to the motion of the electrons and holes are depicted individually, as is the total collected charge. It is noted that the charge related to the motion of holes exceeds to that related to the motion of the electrons by a factor of about 1.416. This might

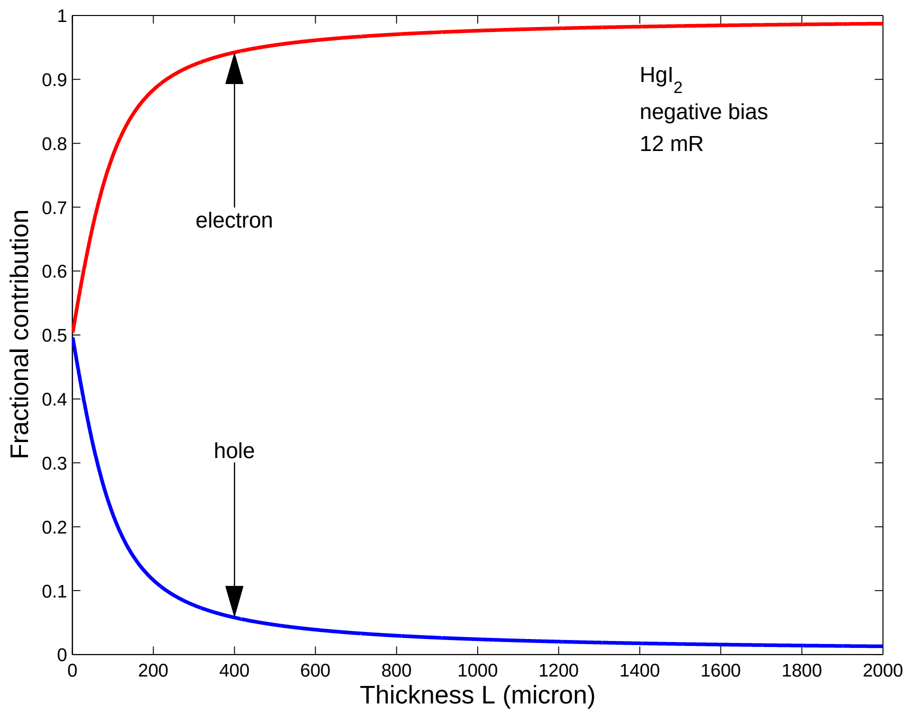

Figure 4.22: The fractional contributions to the collected charge per unit area related to the motion of the electrons and holes for a HgI_2 based X-ray imager for the electric field strength set to 100 kV/cm for the case of negative bias. The X-ray flux, X, is set to 12 mR. These results are plotted as a function of the imager thickness. These results correspond to the results presented in Figure 4.21. Eqs. (3.12), (3.14), and (3.15) are used to generate this plot. The online version of the figure is in color.

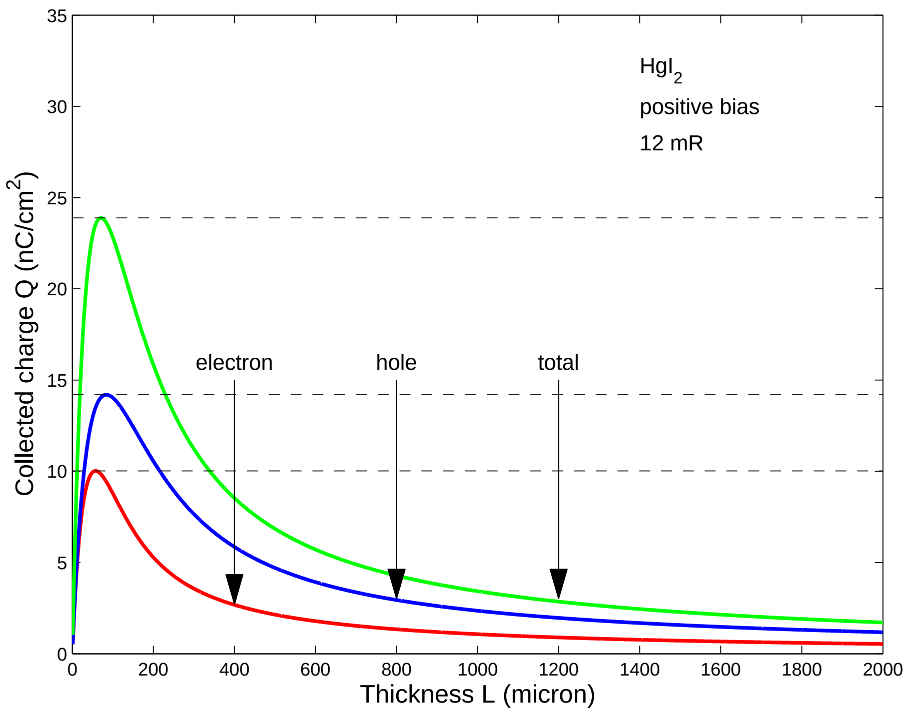

Figure 4.23: The collected charge per unit area as a function of the thickness of the X-ray imager for the case of a HgI_2 based X-ray imager, for the electric field strength set to 100 kV/cm for the case of positive bias. The X-ray flux, X, is set to 12 mR. The collected charge per unit area related to the motion of electrons and holes are depicted, as is the total collected charge, which of course is equal to the sum of that due to the motion of the electrons and holes. The corresponding no trapping limits, depicted with the dashed lines, are also shown. Eqs. (3.15), (3.16), and (3.17) are used to generate this plot. The online version of the figure is in color.

have been expected as holes, on average, will drift longer before they reach the terminal electrode while electrons drift a shorter distance; recall Ramos theorem. It is also noted that the amount of collected charge monotonically increases with imager thickness and achieves a maximum, and then monotonically decreases in response to further increase in the thickness of the X-ray imager, i.e., there is a opportunity to collect maximum number of charge at a particular thickness of the X-ray imager. By taking the no-trapping limits, both associated with the motion of the electrons and holes, upper bounds on the charge collection per unit area may be obtained associated with the motion of the electrons and holes, and the corresponding total collected charge. The fractional contributions to the collected charge per unit area related to the motion of the electrons and holes, corresponding to the functional dependence depicted in Figure 4.23, are presented in Figure 4.24. As expected, the motion of the holes is the dominant contribution to the collected charge per unit area for this particular case.

4.3.4 Imager results using PbI_2

In Figure 4.25, the collected charge per unit area associated with a PbI_2 based X-ray imager is plotted as a function of the applied electric field strength for the case of the imager thickness being set to 83 μm, this result corresponding to the application of a negative bias. The collected charge per unit area related to the motion of the electrons and holes are depicted individually, as is the total collected charge. It is noted that the charge related to the motion of electrons exceeds to that related to the motion of the holes by a factor of about 2.5217. This might have been expected as electrons,

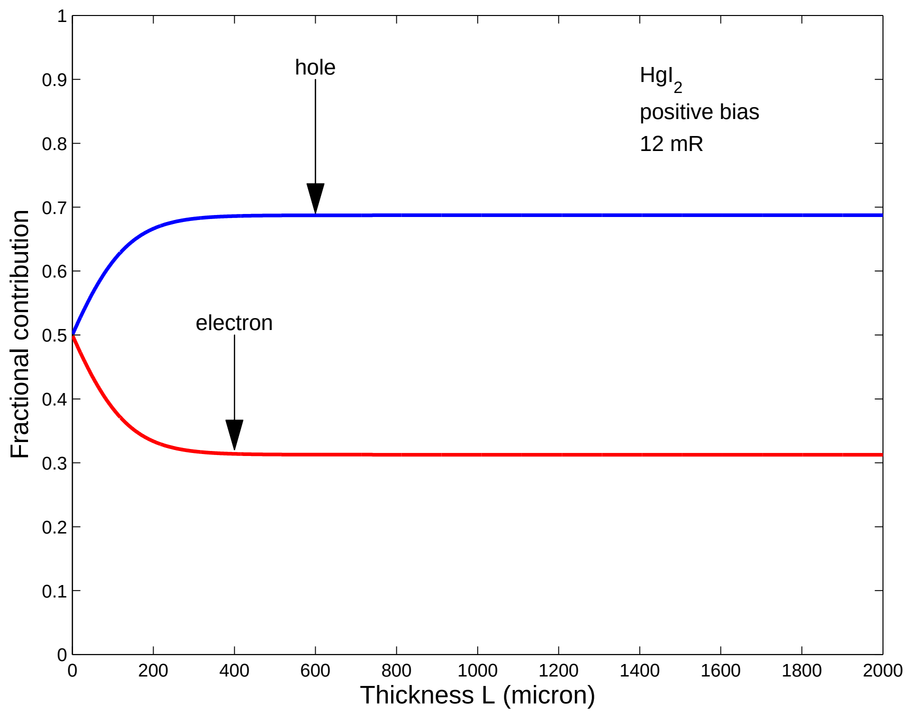

Figure 4.24: The fractional contributions to the collected charge related to the motion of the electrons and holes for a HgI_2 based X-ray imager for the electric field strength set to 100 kV/cm for the case of positive bias. The X-ray flux, X, is set to 12 mR. These results are plotted as a function of the imager thickness. These results correspond to the results presented in Figure 4.23. Eqs. (3.15), (3.16), and (3.17) are used to generate this plot. The online version of the figure is in color.

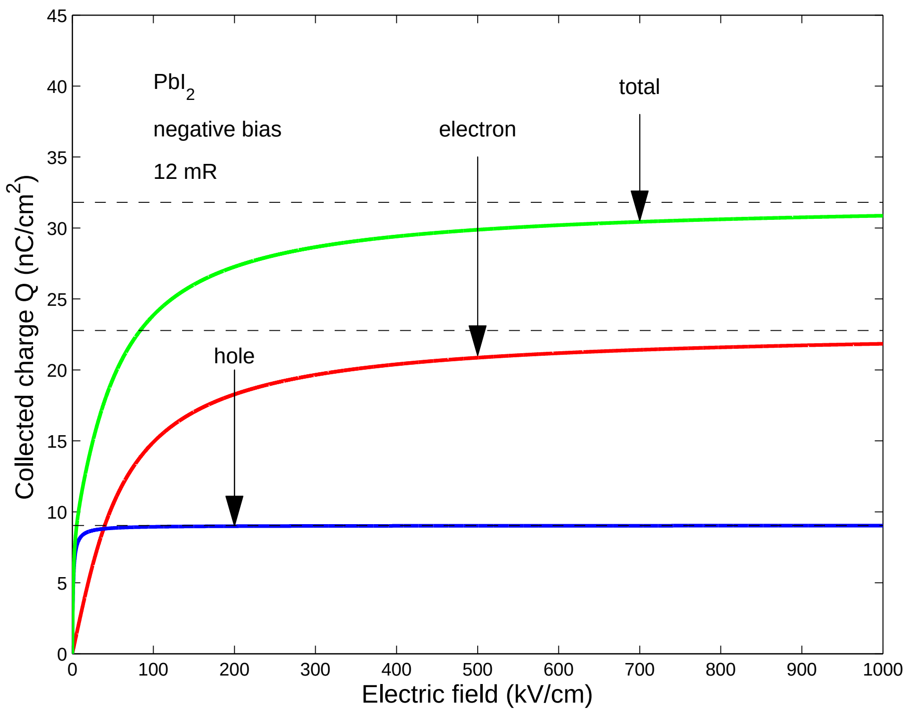

Figure 4.25: The collected charge per unit area as a function of the applied field strength for the case of a PbI_2 based X-ray imager, for the imager thickness set to 83 μm for the case of negative bias. The X-ray flux, X, is set to 12 mR. The collected charge related to the motion of the electron and hole individually shown, as is the total charge, which of course is equal to the sum of that due to the motion of the electrons and holes. The corresponding no trapping limits, depicted with the dashed lines, are also shown. Eqs. (3.12), (3.14), and (3.15) are used to generate this plot. The online version of the figure is in color.

on average, will drift longer before they reach the terminal electrode while holes drift a shorter distance; recall Ramo's theorem. It is also noted that the collected charge monotonically increases with the applied electric field strength, i.e., there are less opportunities for trapping if the charge carriers are moving faster. By taking the no-trapping limits, both associated with the motion of the electrons and the holes, upper bounds on the charge collection per unit area may be obtained, both associated with the motion of electrons and holes, and the corresponding total collected charge. The fractional contributions to the collected charge per unit area, related to the motion of the electrons and holes, corresponding to the functional dependencies depicted in Figure 4.25, are presented in Figure 4.26. As expected, the motion of electrons is the dominant contribution to the collected charge per unit area for this particular case.

In Figure 4.27, the collected charge per unit area associated with a PbI_2 based X-ray imager is plotted as a function of the applied electric field strength for the case of the imager thickness being set to 83 μm, this result corresponding to the application of a positive bias. The collected charge per unit area related to the motion of the electrons and holes are depicted individually, as is the total collected charge. It is noted that the charge related to the motion of holes exceeds that related to the motion of the electrons by a factor of about 2.54. This might have been expected as holes, on average, will drift longer before they reach the terminal electrode while electrons drift a shorter distance; recall Ramos theorem. It is also noted that the collected charge per unit area monotonically increases with the applied electric field strength, i.e., there are less opportunities for trapping if the

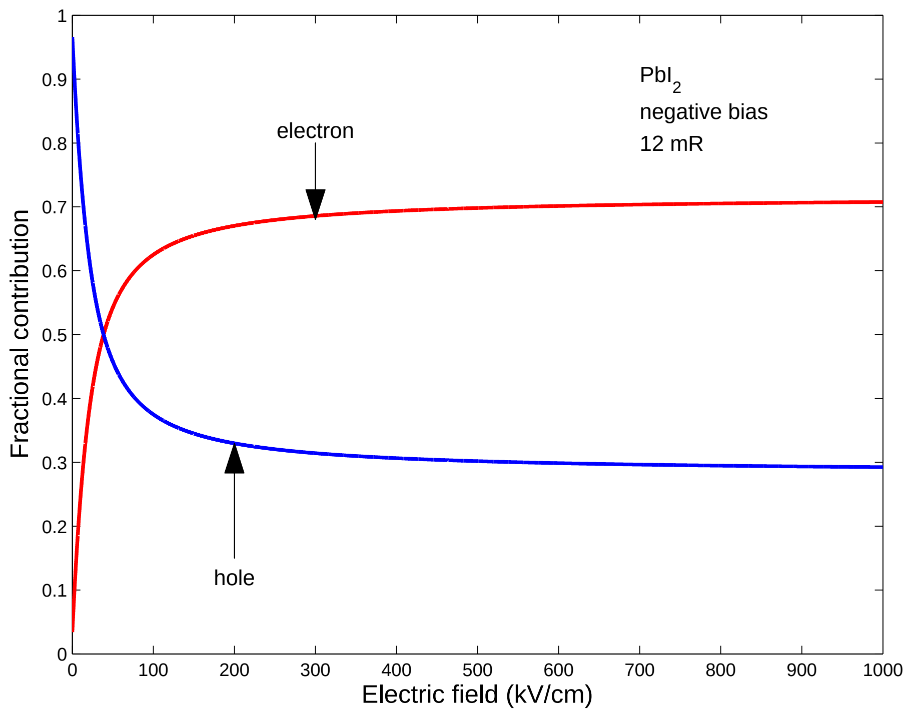

Figure 4.26: The fractional contributions to the collected charge related to the motion of the electrons and holes for a PbI_2 based X-ray imager for the imager thickness set to 83 μm for the case of negative bias. The X-ray flux, X, is set to 12 mR. These results are plotted as a function of the applied electric field strength. These results correspond to the results presented in Figure 4.25. Eqs. (3.12), (3.14), and (3.15) are used to generate this plot. The online version is in color.

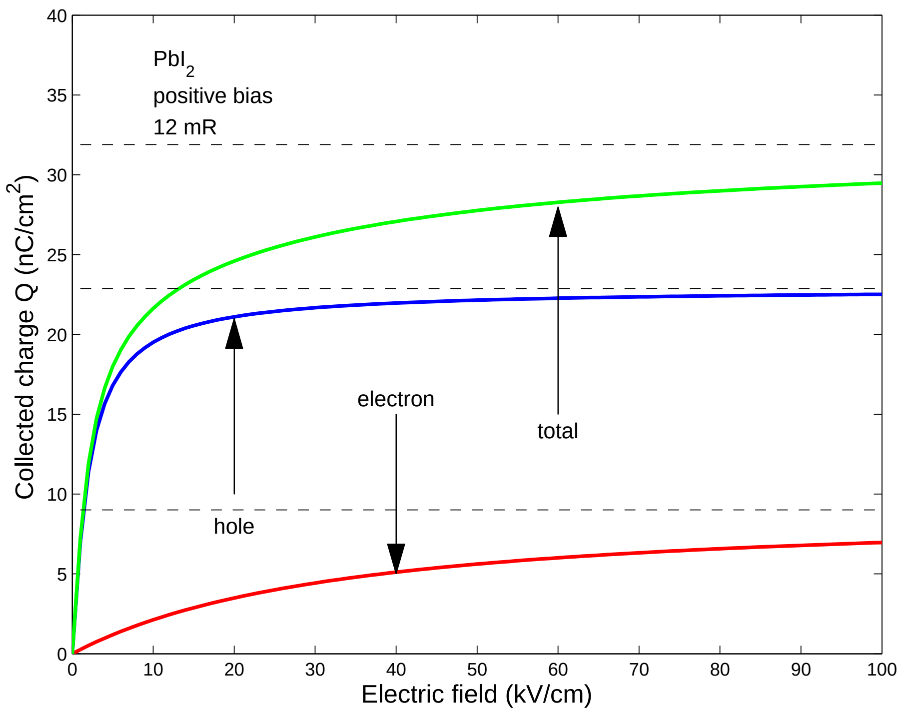

Figure 4.27: The collected charge per unit area as a function of the applied electric field strength for the case of a PbI_2 based X-ray imager for the imager thickness set to 83 μm for the case of positive bias. The X-ray flux, X, is set to 12 mR. The collected charge per unit area related to the motion of electrons and holes are depicted, as is the total collected charge per unit area, which of course is equal to the sum of that due to the motion of the electrons and holes. The corresponding no trapping limits, depicted with the dashed lines, are also shown. Eqs. (3.15), (3.16), and (3.17) are used to generate this plot. The online version of the figure is in color.

charge carriers are moving faster. By taking the no-trapping limits, both associated with the motion of the electrons and the holes, upper bounds on the charge collection per unit area may be obtained, both associated with the motion of the electrons and holes, and the corresponding total collected charge. The fractional contributions to the collected charge per unit area, related to the motion of the electrons and holes, corresponding to the functional dependencies depicted in Figure 4.27, are presented in Figure 4.28. As expected, the motion of holes is the dominant contribution to the collected charge per unit area for this particular case.

In Figure 4.29, the collected charge per unit area associated with a PbI_2 based X-ray imager is plotted as a function of the imager thickness for the case of electric field strength being set to 100 kV/cm, this result corresponding to the application of a negative bias. The collected charge per unit area related to the motion of the electrons and holes are depicted individually, as is the total collected charge per unit area. It is noted that the charge related to the motion of electrons exceeds that related to the motion of the holes by a factor of about 1.49. This might have been expected as electrons, on average, will drift longer before they reach the terminal electrode while holes drift a shorter distance; recall Ramos theorem. It is also noted that the amount of collected charge per unit area initially monotonically increases with the imager thickness, achieves a maximum, and then monotonically decreases in response to further increase in the X-ray imager thickness, i.e., there is an opportunity to collect a maximum amount of charge per unit area at a particular thickness of the imager. By taking the no-trapping limits, both associated with the motion of the electrons and holes, upper bounds

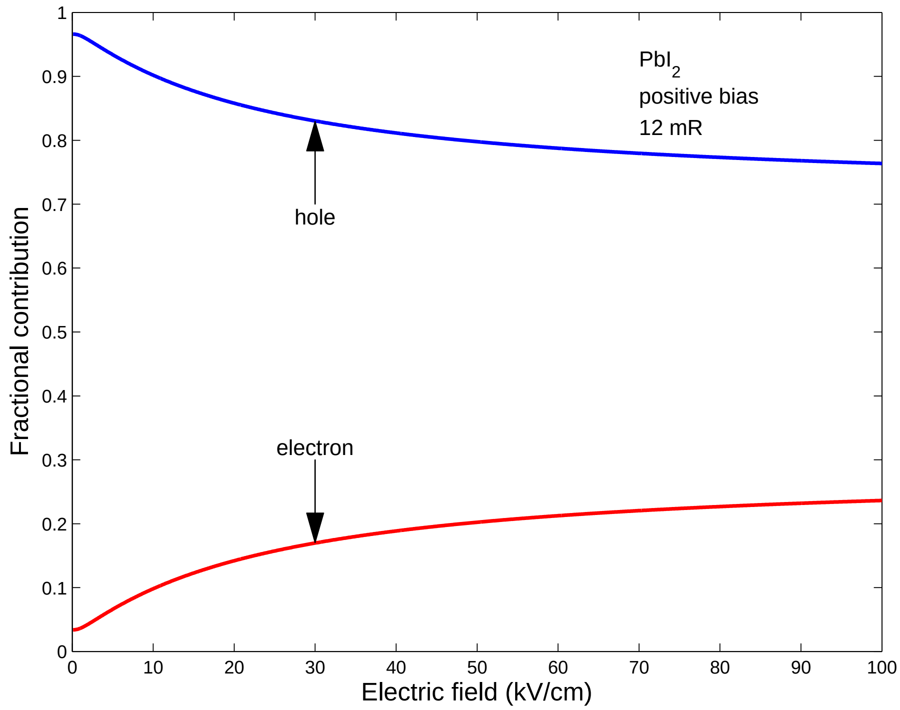

Figure 4.28: The fractional contributions to the collected charge per unit area related to the motion of the electrons and holes for a PbI_2 based X-ray imager for the imager thickness set to 83 μm for the case of a positive bias. The X-ray flux, X, is set to 12 mR. These results are plotted as a function of the applied electric field strength. These results correspond to the results presented in Figure 4.27. Eqs. (3.15), (3.16), and (3.17) are used to generate this plot. The online version is in color.

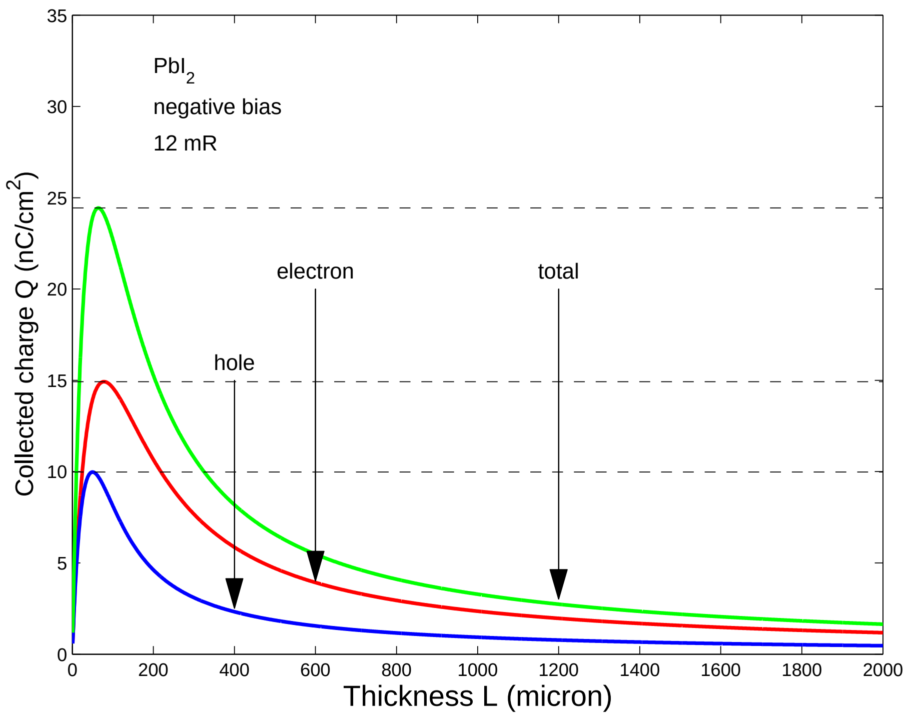

Figure 4.29: The collected charge per unit area as a function of the thickness of the X-ray imager for the case of a PbI_2 based X-ray imager for the electric field strength set to 100 kV/cm for the case of negative bias. The X-ray flux, X, is set to 12 mR. The collected charge per unit area related to the motion of the electrons and the holes are depicted, as is the total collected charge, which of course is equal to the sum of that due to the motion of the electrons and holes. The corresponding no trapping limits, depicted with the dashed lines, are also shown. Eqs. (3.12), (3.14), and (3.15) are used to generate this plot. The online version of the figure is in color.

on the charge collection per unit area may be obtained associated with the motion of the electrons and the holes, and the corresponding total collected charge per unit area. The fractional contributions to the collected charge per unit area, related to the motion of the electrons and holes, corresponding to the functional dependencies depicted in Figure 4.29, are presented in Figure 4.30. As expected, the motion of the electrons is the dominant contribution to the collected charge per unit area for this particular case.

In Figure 4.31, the collected charge per unit area associated with a PbI_2 based X-ray imager is plotted as a function of the X-ray imager thickness for the case of the electric field strength being set to 100 kV/cm for the case of positive bias. The collected charge per unit area related to the motion of the electrons and holes are depicted individually, as is the total collected charge. It is noted that the charge related to the motion of holes exceeds to that related to the motion of the electrons by a factor of about 7.79. This might have been expected as holes, on average, will drift longer before they reach the terminal electrode while electrons drift a shorter distance; recall Ramos theorem. It is also noted that the amount of collected charge monotonically increases with imager thickness and achieves a maximum, and then monotonically decreases in response to further increase in the thickness of the X-ray imager, i.e., there is a opportunity to collect maximum number of charge at a particular thickness of the X-ray imager. By taking the no-trapping limits, both associated with the motion of the electrons and holes, upper bounds on the charge collection may be obtained associated with the motion of the electrons and holes, and the corresponding total collected charge. The fractional contributions to the collected charge per

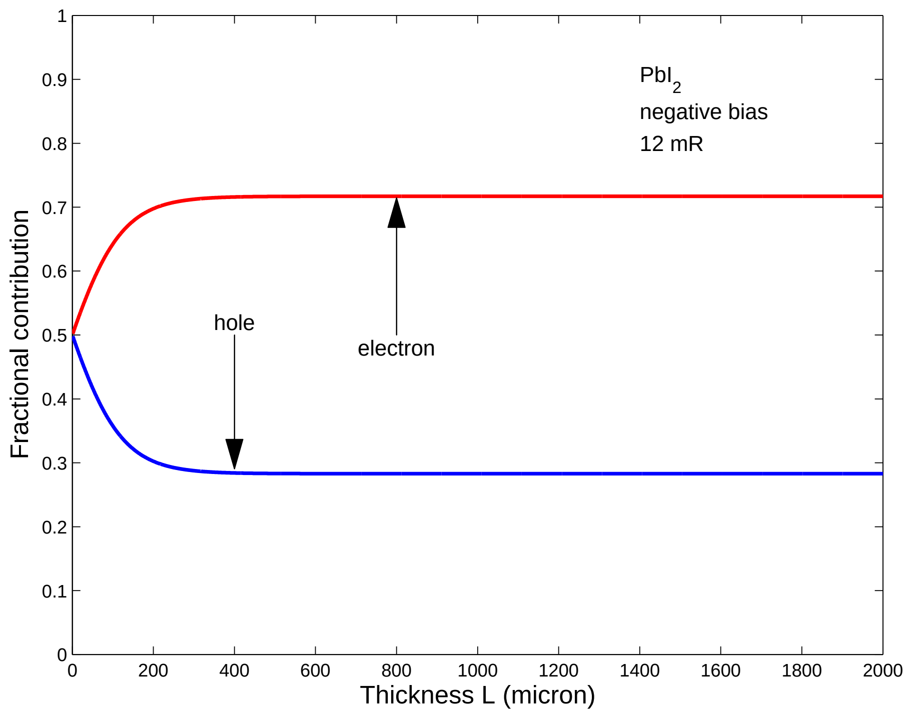

Figure 4.30: The fractional contributions to the collected charge per unit area related to the motion of the electrons and holes for a PbI_2 based X-ray imager for the electric field strength set to 100 kV/cm for the case of negative bias. The X-ray flux, X, is set to 12 mR. These results are plotted as a function of the imager thickness. These results correspond to the results presented in Figure 4.29. Eqs. (3.12), (3.14), and (3.15) are used to generate this plot. The online version of the figure is in color.

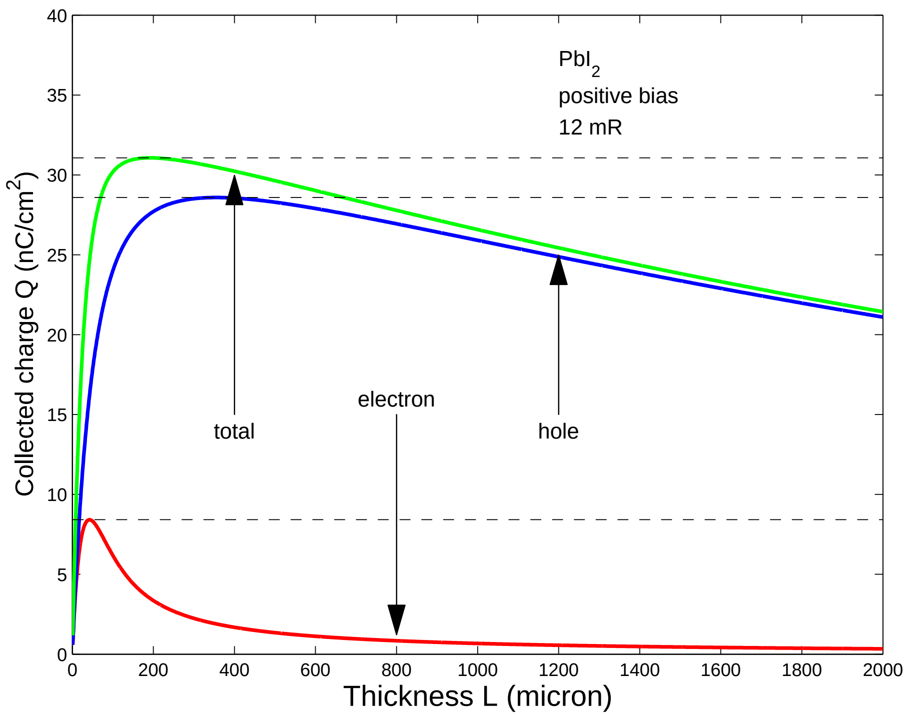

Figure 4.31: The collected charge per unit area as a function of the thickness of the X-ray imager for the case of a PbI_2 based X-ray imager, for the electric field strength set to 100 kV/cm for the case of positive bias. The X-ray flux, X, is set to 12 mR. The collected charge per unit area related to the motion of electrons and holes are depicted, as is the total collected charge, which of course is equal to the sum of that due to the motion of the electrons and holes. The corresponding no trapping limits, depicted with the dashed lines, are also shown. Eqs. (3.15), (3.16), and (3.17) are used to generate this plot. The online version of the figure is in color.

unit area related to the motion of the electrons and holes, corresponding to the functional dependencies depicted in Figure 4.31, are presented in Figure 4.32. As expected, the motion of the holes is the dominant contribution to the collected charge per unit area for this particular case.

4.3.5 Imager results using TlBr

In Figure 4.33, the collected charge per unit area associated with a TlBr based X-ray imager is plotted as a function of the applied electric field strength for the case of the imager thickness being set to 500 μm, this result corresponding to the application of a negative bias. The collected charge per unit area related to the motion of the electrons and holes are depicted individually, as is the total collected charge. It is noted that the charge related to the motion of electrons exceeds that related to the motion of the holes by a factor of about 44.21. This might have been expected as electrons, on average, will drift longer before they reach the terminal electrode while holes drift a shorter distance; recall Ramo's theorem. It is also noted that the collected charge monotonically increases with the applied electric field strength, i.e., there are less opportunities for trapping if the charge carriers are moving faster. By taking the no-trapping limits, both associated with the motion of the electrons and the holes, upper bounds on the charge collection per unit area may be obtained, both associated with the motion of the electrons and holes, and the corresponding total collected charge. The fractional contributions to the collected charge per unit area, related to the motion of the electron and holes, corresponding to the functional dependencies depicted in Figure 4.33, are presented in Figure

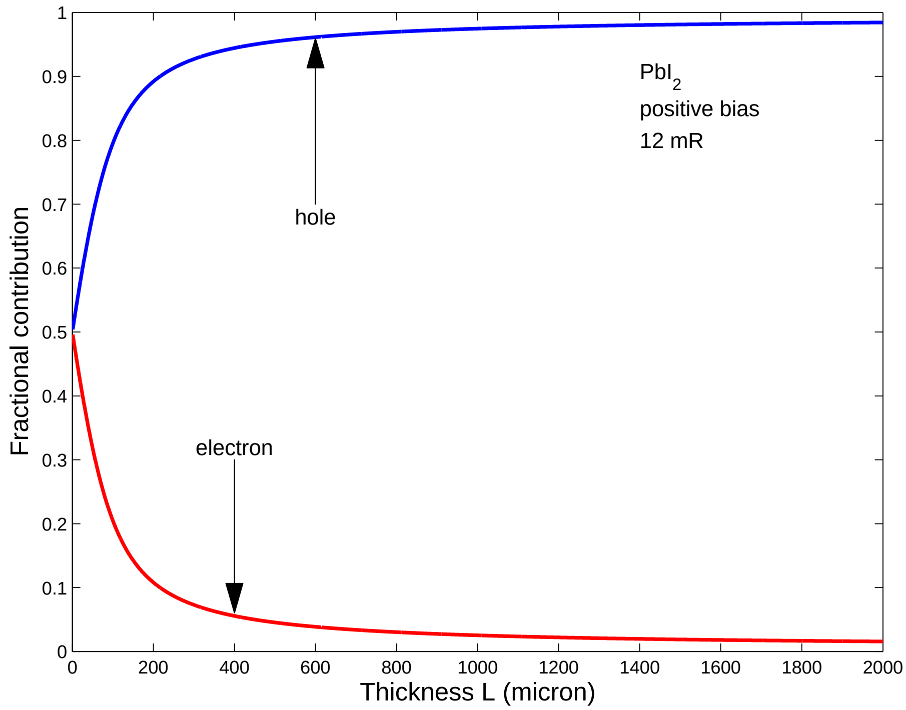

Figure 4.32: The fractional contributions to the collected charge per unit area related to the motion of the electrons and holes for a PbI_2 based X-ray imager for the electric field strength set to 100 kV/cm for the case of positive bias. The X-ray flux, X, is set to 12 mR. These results are plotted as a function of the imager thickness. These results correspond to the results presented in Figure 4.31. Eqs. (3.15), (3.16), and (3.17) are used to generate this plot. The online version of the figure is in color.

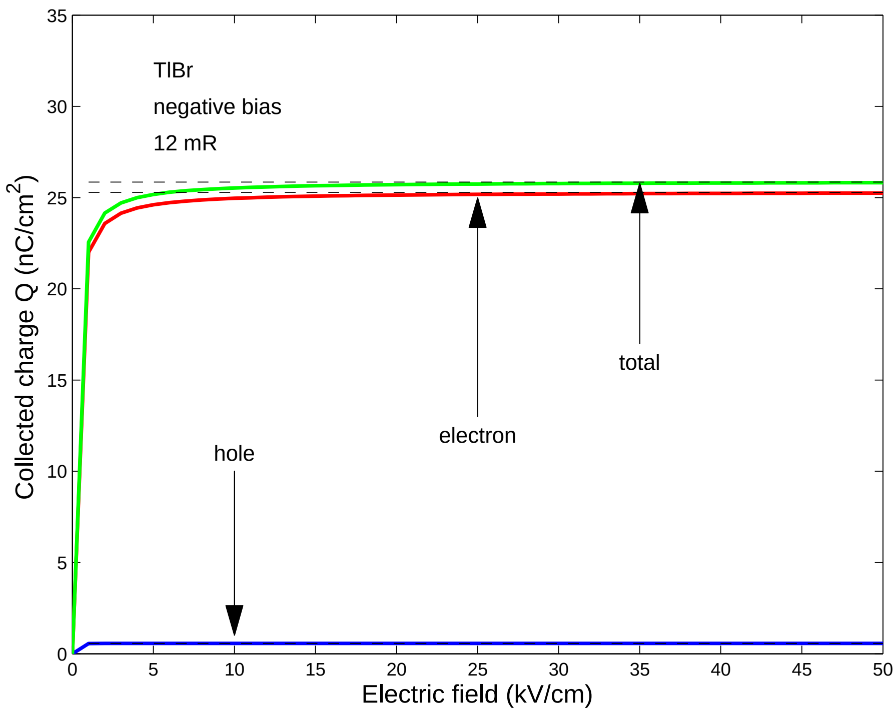

Figure 4.33: The collected charge per unit area as a function of the applied field strength for the case of a TlBr based X-ray imager, for the imager thickness set to 500 μm for the case of negative bias. The X-ray flux, X, is set to 12 mR. The collected charge per unit area related to the motion of the electron and hole individually shown, as is the total charge, which of course is equal to the sum of that due to the motion of the electrons and holes. The corresponding no trapping limits, depicted with the dashed lines, are also shown. Eqs. (3.12), (3.14), and (3.15) are used to generate this plot. The online version of the figure is in color.

4.34. As expected, the motion of electrons is the dominant contribution to the collected charge per unit area for this particular case.

In Figure 4.35, the collected charge per unit area associated with a TlBr based X-ray imager is plotted as a function of the applied electric field strength for the case of the imager thickness being set to 500 μm, this result corresponding to the application of a positive bias. The collected charge related to the motion of the electrons and holes are depicted individually, as is the total collected charge. It is noted that the charge related to the motion of holes exceeds that related to the motion of the electrons by a factor of about 44.43. This might have been expected as holes, on average, drift longer before they reach the terminal electrode while electrons drift a shorter distance; recall Ramos theorem. It is also noted that the collected charge monotonically increases with the applied electric field strength, i.e., there are less opportunities for trapping if the charge carriers are moving faster. By taking the no-trapping limits, both associated with the motion of the electrons and holes, upper bounds on the charge collection per unit area may be obtained, both associated with the motion of electrons and holes, and the corresponding total collected charge. The fractional contributions to the collected charge per unit area, related to the motion of the electrons and holes, corresponding to the functional dependencies depicted in Figure 4.35, are presented in Figure 4.36. As expected, the motion of holes is the dominant contribution to the collected charge per unit area for this particular case.

In Figure 4.37, the collected charge per unit area associated with a TlBr based X-ray imager is plotted as a function of the imager thickness for the

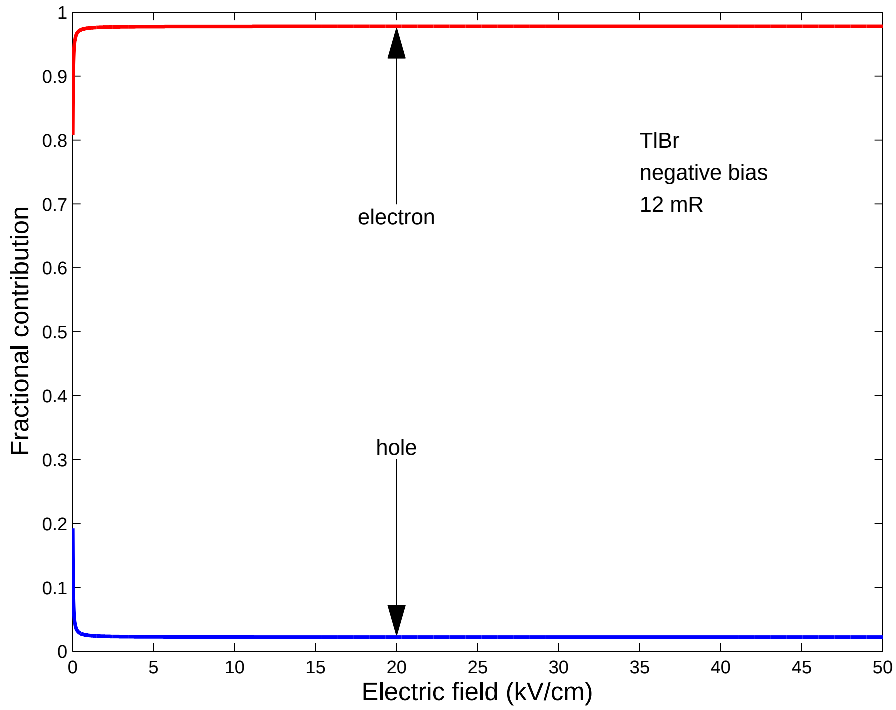

Figure 4.34: The fractional contributions to the collected charge per unit area related to the motion of the electrons and holes for a TlBr based X-ray imager for the imager thickness set to 500 μm for the case of negative bias. The X-ray flux, X, is set to 12 mR. These results are plotted as a function of the applied electric field strength. These results correspond to the results presented in Figure 4.33. Eqs. (3.12), (3.14), and (3.15) are used to generate this plot. The online version is in color.

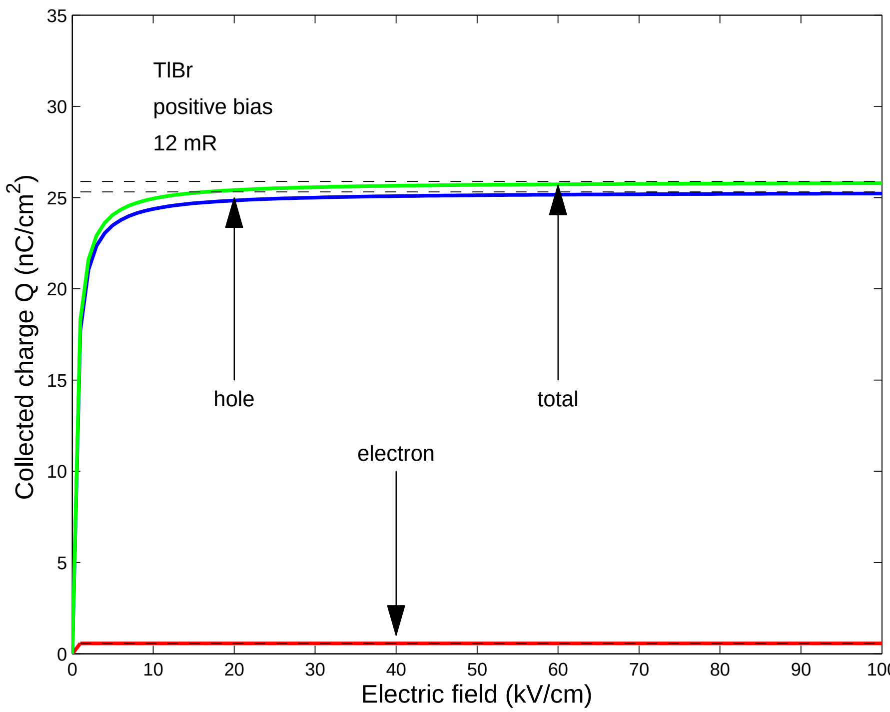

Figure 4.35: The collected charge per unit area as a function of the applied electric field strength for the case of a TlBr based X-ray imager for the imager thickness set to 500 μm for the case of positive bias. The X-ray flux, X, is set to 12 mR. The collected charge related to the motion of electrons and holes are depicted, as is the total collected charge, which of-course is equal to the sum of that due to the motion of the electrons and holes. The corresponding no trapping limits, depicted with the dashed lines, are also shown. Eqs. (3.15), (3.16), and (3.17) are used to generate this plot. The online version of the figure is in color.

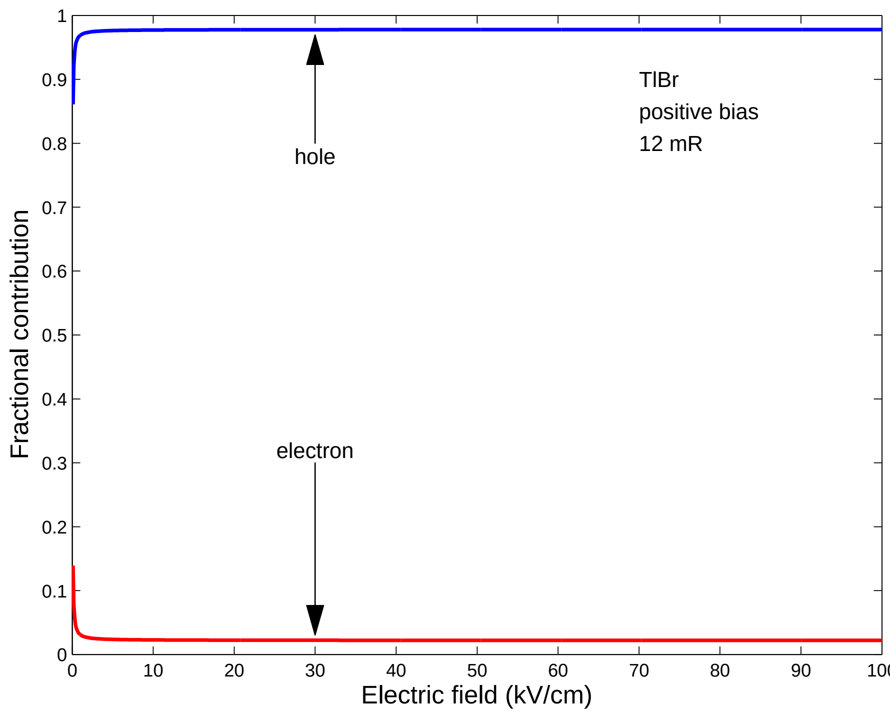

Figure 4.36: The fractional contributions to the collected charge per unit area related to the motion of the electrons and holes for a TlBr based X-ray imager for the imager thickness set to 500 μm for the case of a positive bias. The X-ray flux, X, is set to 12 mR. These results are plotted as a function of the applied electric field strength. These results correspond to the results presented in Figure 4.35. Eqs. (3.15), (3.16), and (3.17) are used to generate this plot. The online version is in color.

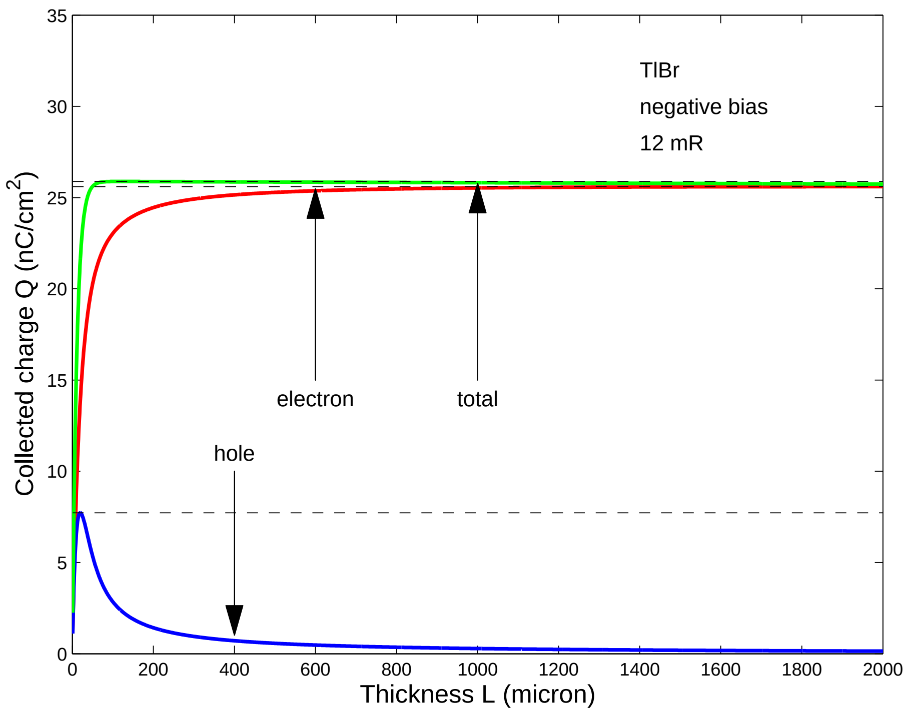

Figure 4.37: The collected charge as a function of the thickness of the X-ray imager for the case of a TlBr based X-ray imager for the electric field strength set to 100 kV/cm for the case of negative bias. The X-ray flux, X, is set to 12 mR. The collected charge related to the motion of the electrons and the holes are depicted, as is the total collected charge, which of course is equal to the sum of that due to the motion of the electrons and holes. The corresponding no trapping limits, depicted with the dashed lines, are also shown. Eqs. (3.12), (3.14), and (3.15) are used to generate this plot. The online version of the figure is in color.

case of the electric field strength being set to 100 kV/cm, this result corresponding to the application of a negative bias. The collected charge per unit area related to the motion of the electrons and holes are depicted individually, as is the total collected charge. It is noted that the charge related to the motion of electrons exceeds that related to the motion of the holes by a factor of about 9.455. This might have been expected as electrons, on average, will drift longer before they reach the terminal electrode while holes drift a shorter distance; recall Ramos theorem. It is also noted that the collected charge monotonically increases with the imager thickness, and achieves a maximum, and then monotonically decreases in response to further increase in the imager thickness, i.e., there is an opportunity to collect a maximum number of charge at a particular thickness of the X-ray imager. By taking the no-trapping limits, both associated with the motion of the electrons and holes, upper bounds on the charge collection per unit area may be obtained, associated with the motion of the electrons and holes, and the corresponding total collected charge. The fractional contributions to the collected charge per unit area, related to the motion of the electrons and holes, corresponding to the functional dependencies depicted in Figure 4.37, are presented in Figure 4.38. As expected, the motion of the electrons is the dominant contribution to the collected charge per unit area for this particular case.

In Figure 4.39, the collected charge per unit area associated with a TlBr based X-ray imager is plotted as a function of the X-ray imager thickness for the case of the electric field strength being set to 100 kV/cm for the case of positive bias. The collected charge per unit area related to the motion

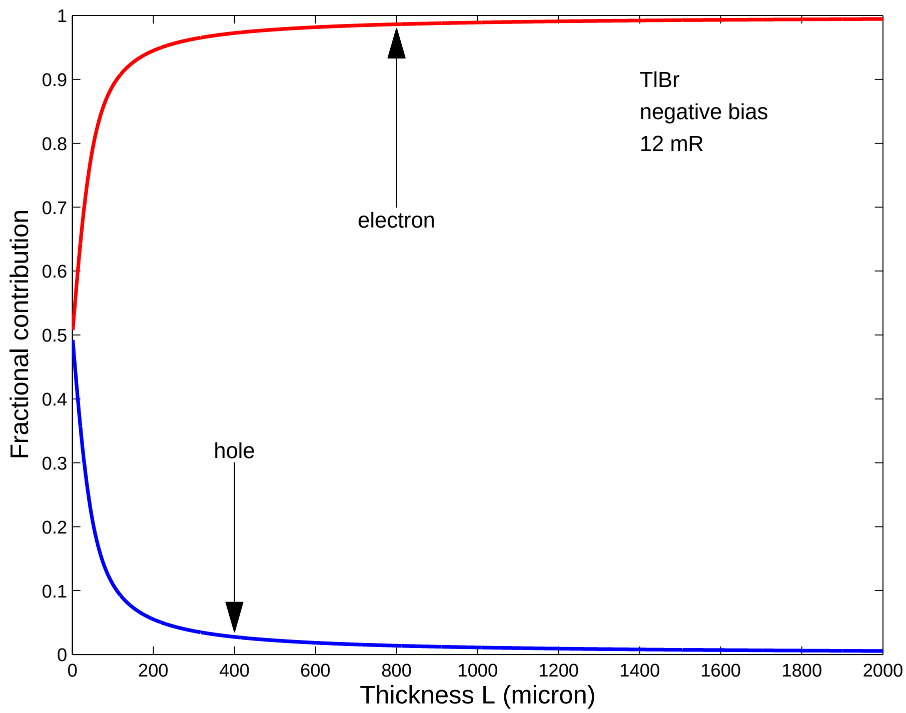

Figure 4.38: The fractional contributions to the collected charge per unit area related to the motion of the electrons and holes for a TlBr based X-ray imager for the electric field strength set to 100 kV/cm for the case of negative bias. The X-ray flux, X, is set to 12 mR. These results are plotted as a function of the imager thickness. These results correspond to the results presented in Figure 4.37. Eqs. (3.12), (3.14), and (3.15) are used to generate this plot. The online version of the figure is in color.

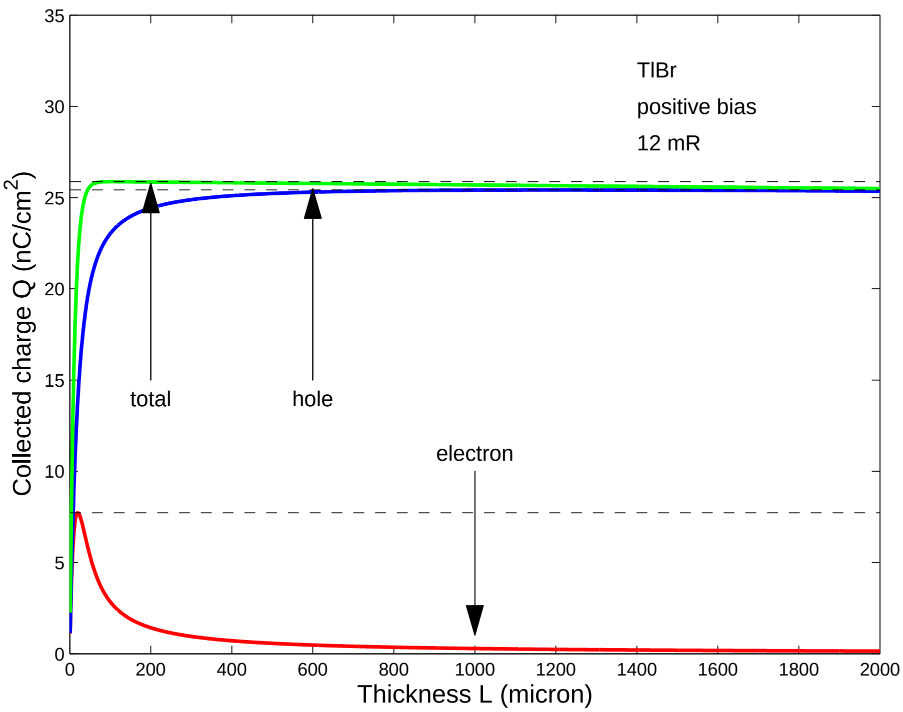

Figure 4.39: The collected charge per unit area as a function of the thickness of the X-ray imager for the case of a TlBr based X-ray imager, for the electric field strength set to 100 kV/cm for the case of positive bias. The X-ray flux, X, is set to 12 mR. The collected charge per unit area related to the motion of electrons and holes are depicted, as is the total collected charge, which of course is equal to the sum of that due to the motion of the electrons and holes. The corresponding no trapping limits, depicted with the dashed lines, are also shown. Eqs. (3.15), (3.16), and (3.17) are used to generate this plot. The online version of the figure is in color.

of the electrons and holes are depicted individually, as is the total collected charge. It is noted that the charge related to the motion of holes exceeds to that related to the motion of the electrons by a factor of about 8.09. This might have been expected as holes, on average, will drift longer before they reach the terminal electrode while electrons drift a shorter distance; recall Ramos theorem. It is also noted that the amount of collected charge monotonically increases with imager thickness and achieves a maximum, and then monotonically decreases in response to further increase in the thickness of the X-ray imager, i.e., there is an opportunity to collect maximum number of charge at a particular thickness of the X-ray imager. By taking the no-trapping limits, both associated with the motion of the electrons and holes, upper bounds on the charge collection per unit area may be obtained associated with the motion of the electrons and holes, and the corresponding total collected charge. The fractional contributions to the collected charge per unit area related to the motion of the electrons and holes, corresponding to the functional dependencies depicted in Figure 4.39, are presented in Figure 4.40. As expected, the motion of the holes is the dominant contribution to the collected charge per unit area for this particular case.

4.4 Comparative analysis

A critical comparison between the results is now presented. In Figure 4.41, the collected charge per unit area is plotted as a function of the electric field for the case of the five X-ray photoconductors considered in this analysis, i.e., a-Se, CdZnTe, HgI_2, PbI_2, and TlBr, for the case of negative

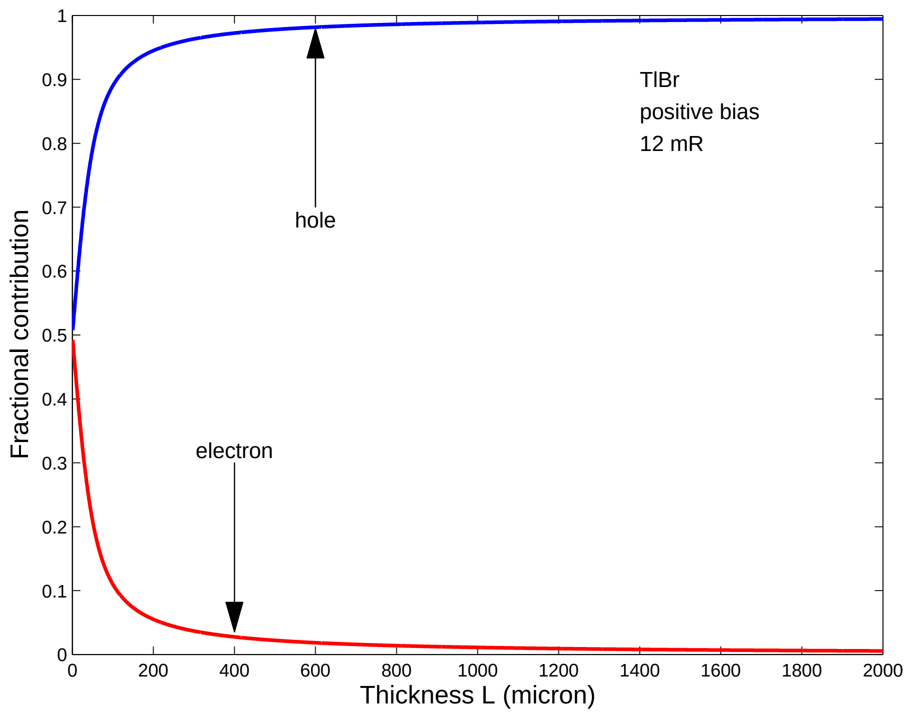

Figure 4.40: The fractional contributions to the collected charge per unit area related to the motion of the electrons and holes for a TlBr based X-ray imager for the electric field strength set to 100 kV/cm for the case of positive bias. The X-ray flux, X, is set to 12 mR. These results are plotted as a function of the imager thickness. These results correspond to the results presented in Figure 4.39. Eqs. (3.15), (3.16), and (3.17) are used to generate this plot. The online version of the figure is in color.

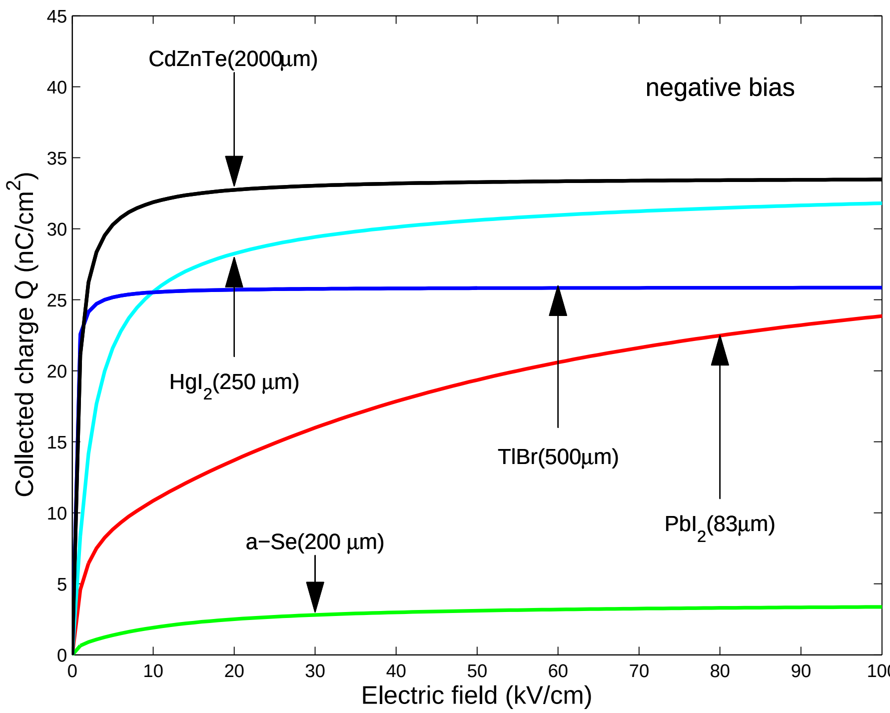

Figure 4.41: The collected charge per unit area plotted as a function of the electric field for the case of five X-ray photoconductors considered in this analysis for the case of negative bias. The X-ray flux, X, is set to 12 mR. Eqs. (3.12), (3.14), and (3.15) are used to generate this plot. The online version of the figure is in color.

bias. It is noted that, for all cases, CdZnTe allows for the greatest amount of collected charge per unit area. This is primarily on account of its small electron-hole creation energy, $W_{\pm}$. An analogous result is depicted in Figure 4.42 for the case of positive bias.

In Figure 4.43, the collected charge per unit area is plotted as a function of the thickness of the X-ray photoconductor as a function of the detector thickness for the case of the five X-ray photoconductors considered in this analysi, i.e., a-Se, CdZnTe, HgI_2, PbI_2, and TlBr, for the case of negative bias. For all cases, this collected charge corresponds to the motion of both types of charge carriers. It is noted that CdZnTe has a greater amount of collected charge per unit area than any other X-ray photoconductor considered in this analysis. An analogous result is depicted in Figure 4.44 for the case of positive bias.

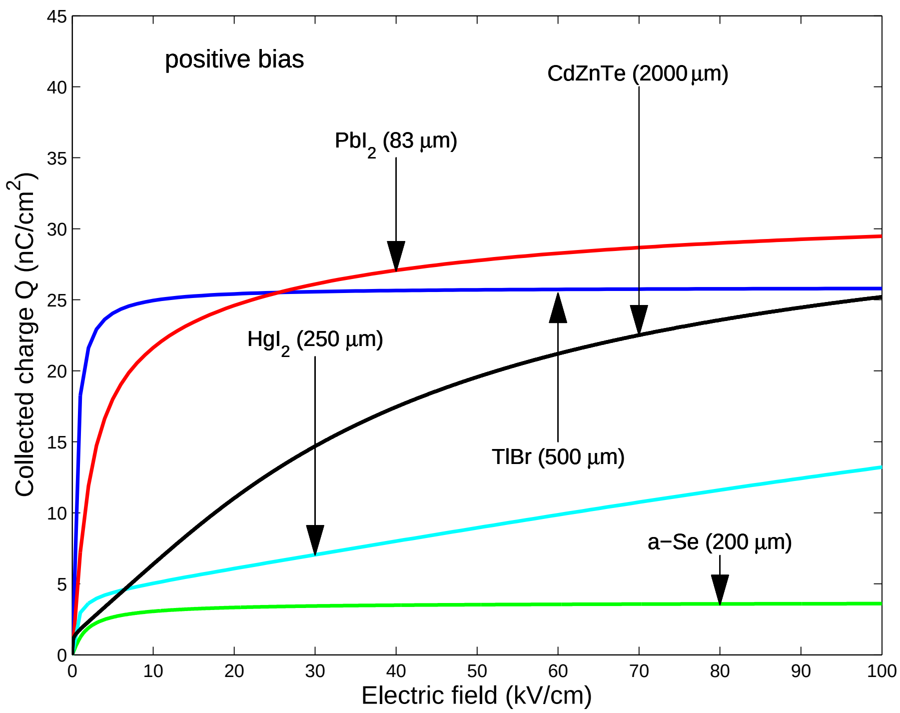

Figure 4.42: The collected charge per unit area plotted as a function of the applied electric field for the case of the five X-ray photoconductors considered in this analysis for the case of positive bias. The X-ray flux, X, is set to 12 mR for all cases. Eqs. (3.15), (3.16), and (3.17) are used to generate this plot. The online version of the figure is in color.

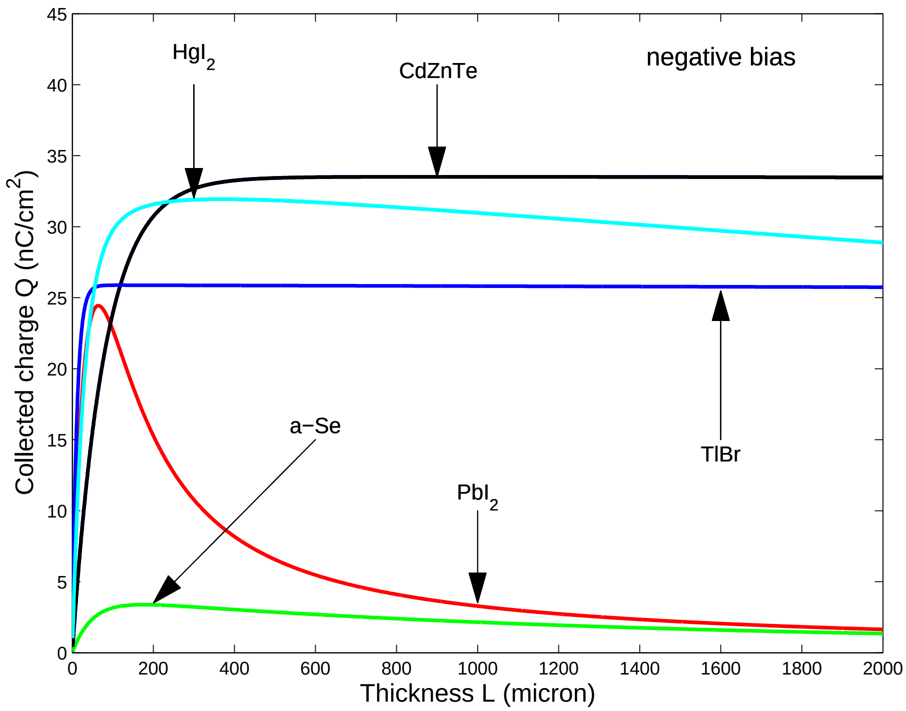

Figure 4.43: The collected charge per unit area plotted as a function of the thickness of the X-ray photoconductor for the five X-ray photoconductors considered in this analysis for the case of negative bias. The electric field is being set to 100 kV/cm. The X-ray flux, X, is set to 12 mR for all cases. Eqs. (3.12), (3.14), and (3.15) are used to generate this plot. The online version is in color.

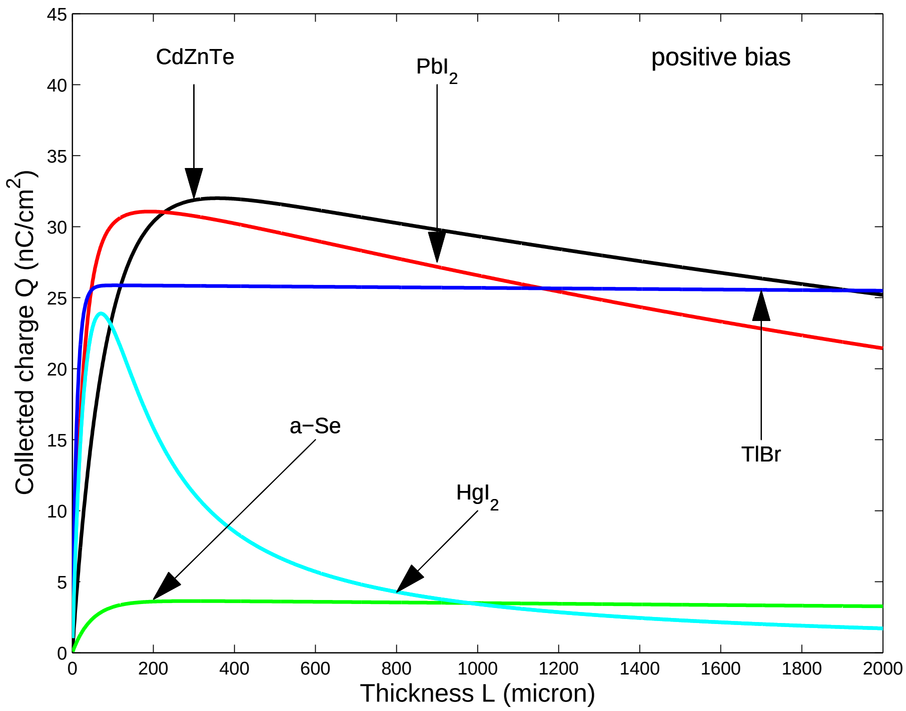

Figure 4.44: The collected charge per unit area plotted as a function of the thickness of the X-ray photoconductor for the case of five X-ray photoconductors considered in this analysis for the case of positive bias. The electric field is being set to 100 kV/cm. The X-ray flux, X, is set to 12 mR for all cases. Eqs. (3.15), (3.16), and (3.17) are used to generate this plot. The online version is in color.

Chapter 5

Conclusions

In this thesis, the performance of direct-conversion digital X-ray imagers was evaluated using an elementary model that draws upon the material properties and dimensions of the X-ray photoconductor employed. Five possible X-ray photoconductors were considered in this analysis, namely a-Se, CdZnTe, HgI_2, PbI_2, and TlBr. The collected charge per unit area was the performance metric considered in this analysis. The collected charge per unit area related to the motion of the electrons and holes individually, and that due to the motion of both types of charge carriers, was evaluated. The fractional contributions were also evaluated. The application of both positive and negative biases to the radiation receiving terminals were considered. It was found that the collected charge per unit area for the case of both positive and negative bias, is higher in CdZnTe, when compared to other materials considered in this analysis. This suggests that CdZnTe is the better material in case of amount charge collected per unit area.

This thesis presents a number of original contributions that add onto the understanding of the performance of direct-conversion digital X-ray imagers. While the results presented are based upon the analytical expressions provided by Kabir and Kasap [11], there are number of novel aspects to this analysis which distinguish it from that of Kabir and Kasap [11]. The evaluation of the performance of such an imager with respect to the different materials considered in this analysis was not performed by Kabir and Kasap [11], and represents a useful contribution to the field. This is particularly true with regards to the performance comparison results that were presented in Section 4.4. The identification of the individual contributions to the collected charge attributable to the electrons and holes is another novel aspect of this analysis.

There area a variety of topics that could be considered for possible future work. Recombination effects, between the electrons and holes, something not considered in this analysis could play an important role in shaping the resultant device performance. The finiteness of the trapping that can occur, something not considered in this analysis, also has the potential to shape device performance. Finally, a comparison with the results of the experimental work would be a useful contribution to the field. These topics will have to be dealt with in the future.

References

[1] O. W. Linton, "Medical applications of X-rays," *Beam Line*, vol. 25, no. 2, pp. 25-34, 1995.

[2] W. C. Röntgen, "On a new kind of rays," *Science*, vol. 3, no. 59, pp. 227-231, 1896.

[3] S. K. O'Leary, "Digital Flat Panel X-Ray Image Detectors using Amorphous Selenium," presented in Boise State University, Boise, Idaho, U.S.A, July 2002.

[4] M. Yaffe, and J. A. Rowlands, "X-ray detectors for digital radiography," *Physics in Medicine and Biology*, vol. 42, no. 1, pp. 1, 1997.

[5] G. Bansal, "Digital radiography. A comparison with modern conventional imaging," *Postgraduate Medical Journal*, vol. 82, no. 969, pp. 425-428, 2006.

[6] J. Mort, *Anatomy of Xerography: Its Invention and Evolution*, McFarland, Jefferson, 1989.

[7] Y. Izumi and O. Teranuma, T. Sato, K. Uehara, H. Okada, S. Tokuda, and T. Sato, "Development of Flat Panel X-ray Image Sensors," *Sharp Technical Journal*, pp. 25-30, 2001.

[8] S. O. Kasap, M. Z. Kabir, and J. A. Rowlands, "Recent advances in X-ray photoconductors for direct conversion X-ray image detectors," *Current Applied Physics*, vol. 6, no. 3, pp. 288-292, 2006.

[9] S. O. Kasap, and J. A. Rowlands, "Direct-conversion flat-panel X-ray image sensors for digital radiograph," *Proceedings of the IEEE*, vol. 90, no. 4, pp. 591-604, 2002.

[10] R. A. Street, M. Mulato, M. M. Schieber, H. Hermon, K. S. Shah, P. R. Bennett, Y. Dmitryev, J. Ho, R. Lau, E. Meerson, S. E. Ready, B. Reisman, Y. Sado, K. V. Schuylenbergh, A. I. Vilensky, and A. Zuck, "Comparative study of Pbl_2 and Hgl_2 as direct detector materials for high-resolution X-ray image sensors," *Medical Imaging 2001.* International Society for Optics and Photonics, pp. 1-12, 2001.

[11] M. Z. Kabir and S. O. Kasap, "Charge collection and absorption-limited sensitivity of X-ray photoconductors: Applications to a-Se and HgI_2," *Applied Physics Letters*, vol. 80, no. 9, pp. 1664-1666, 2002.

[12] K. Hitomi, M. Matsumoto, O. Muroi, T. Shoji, and Y. Hiratate, "Thallium bromide optical and radiation detectors for X-ray and gamma-ray spectroscopy," *Nuclear Science, IEEE Transactions*, vol. 49, no. 5, pp. 2526-2529, 2002.

[13] S. O. Kasap, M. Z. Kabir, J. A. Rowlands, O. Tousignant, J. Leboeuf, L. Laperriere, and Y. Demers, "Dependence of the detective quantum efficiency of photoconductive X-ray image detectors on charge trans-

port parameters and exposure: Application to a-Se," *Applied Physics Letters*, vol. 81, no. 18, pp. 3482-3484, 2002.

[14] K. Shah, J. Lund, F. Olschner, L. Moy, and M. Squillante, "Thallium bromide radiation detectors," *Nuclear Science, IEEE Transactions*, vol. 36, no. 1, pp. 199-202, 1989.

[15] R. Redus, "Charge Trapping in XR-100T-CdTe and CZT Detectors," *Application Note (ANCT-2 Rev 2)* Revised Jan, vol. 9, 2003.

[16] G. Belev, and S. O. Kasap, "Amorphous selenium as an X-ray photoconductor," *Journal of Non-Crystalline Solids*, vol. 345, pp. 484-488, 2004.

[17] S. O. Kasap, and J. A. Rowlands, "Review X-ray photoconductors and stabilized a-Se for direct conversion digital flat-panel X-ray image-detectors," *Journal of Materials Science: Materials in Electronics*, vol. 11(3), pp. 179-198, 2000.

[18] Y. Nemirovsky, A. Ruzin, G. Asa, and J. Gorelik, "Study of the charge collection efficiency of CdZnTe radiation detectors," *Journal of Electronic Materials*, vol. 25, no. 8, pp.1221-1231, 1996.

[19] C. Szeles, "CdZnTe and CdTe materials for X-ray and gamma ray radiation detector applications," *Physica Status Solidi (b)*, vol. 241, no. 3, pp.783-790, 2004.

[20] S.-H. Cho, S.-U. Heo, C.-W. Choi, S.-S. Kang, S.-H. Nam, J.-K. Park, S.-K. Park, "Properties of Polycrystalline HgI_2 Films Fabricated by

Using a Particle in Binder Method," *Journal of Korean Physical Society*, vol. 52, no. 1123, 2008.

[21] R. A. Street, S. E. Ready, L. Melekhov, J. Ho, A. Zuck, and B. N. Breen, "Approaching the theoretical X-ray sensitivity with HgI_2 direct detection image sensors," *Medical Imaging 2002.* International Society for Optics and Photonics, pp. 414-422, 2002.

[22] R. A. Street, J. T. Rahn, S. E. Ready, K. S. Shah, P. R. Bennett, Y. N. Dmitriyev, P. Mei, J.-P. Lu, R. B. Apte, J. Ho, *et al.*, "X-ray imaging using lead iodide as a semiconductor detector," *Medical Imaging 1999.* International Society for Optics and Photonics 1999, pp. 36-47, 1999.

[23] G. Zentai, L. D. Partain, R. Pavlyuchkova, C. Proano, G. F. Virshup, L. Melekhov, A. Zuck, B. N. Breen, O. Dagan, A. Vilensky, *et al.*, "Mercuric iodide and lead iodide x-ray detectors for radiographic and fluoroscopic medical imaging," *Medical Imaging 2003.* International Society for Optics and Photonics 2003, pp. 77-91, 2003.

[24] M. Z. Kabir, "Modeling of x-ray photoconductors for x-ray image detectors," Ph.D. Dissertation, Dept. Elect. Eng., Univ. of Saskatchewan, Saskatoon, Canada, 2005.